

Synthetic Observations of 21 cm H I Line Profiles from Inhomogeneous Turbulent Interstellar H I Gas with Magnetic Field

YASUO FUKUI,¹ TAKAHIRO HAYAKAWA,^{1,2} TSUYOSHI INOUE,¹ KAZUFUMI TORII,³ RYUJI OKAMOTO,¹
KENGO TACHIHARA,¹ TOSHIKAZU ONISHI,² AND KATSUHIRO HAYASHI¹

¹*Department of Physics, Nagoya University, Furo-cho, Chikusa-ku, Nagoya 464-8602, Japan*

²*Department of Physical Science, Osaka Prefecture University, 1-1 Gakuen, Sakai, Osaka 599-8531, Japan*

³*Nobeyama Radio Observatory, National Astronomical Observatory of Japan, 462-2 Nobeyama, Minamimaki, Minamisaku, Nagano 384-1305, Japan*

(Received; Revised; Accepted)

Submitted to

ABSTRACT

We carried out synthetic observations of interstellar atomic hydrogen at 21 cm wavelength by utilizing the magneto-hydrodynamical numerical simulations of the inhomogeneous turbulent interstellar medium (ISM) (Inoue & Inutsuka 2012). The cold neutral medium (CNM) shows significantly clumpy distribution with a small volume filling factor of 3.5%, whereas the warm neutral medium (WNM) distinctly different smooth distribution with a large filling factor of 96.5%. In projection on the sky, the CNM exhibits highly filamentary distribution with a sub-pc width, whereas the WNM shows smooth extended distribution. In the H I optical depth the CNM is dominant and the contribution of the WNM is negligibly small. The CNM has an area covering factor of 30% in projection, while the WNM has a covering factor of 70%. This causes that the emission-absorption measurements toward radio continuum compact sources tend to sample the WNM with a probability of 70%, yielding smaller H I optical depth and smaller H I column density than those of the bulk H I gas. The emission-absorption measurements, which are significantly affected by the small-scale large fluctuations of the CNM properties, are not suitable to characterize the bulk H I gas. Larger-beam emission measurements which are able to fully sample the H I gas will provide a better tool for that purpose, if a reliable proxy for hydrogen column density, possibly dust optical depth and gamma rays, is available. The present results provide a step toward precise measurements of the interstellar hydrogen with $\sim 10\%$ accuracy. This will be crucial in the interstellar physics including identification of the proton-proton interaction in gamma-ray supernova remnants.

Keywords: ISM: atoms — ISM: clouds — radio lines: ISM

1. INTRODUCTION

The main constituent of the interstellar medium (ISM) is atomic hydrogen H I, and the secondary constituents, whose abundance is ten times less than H I, include molecular hydrogen H₂ and atomic helium He over the global volume of the Galactic disk. It is of primary importance to make precise measurement of H I in our understanding of the structure, kinematics and physical conditions of the interstellar medium and the formation of interstellar clouds and stars.

The 21 cm spin flip transition of H I offers a direct method to measure interstellar H I and has been used extensively over the last several decades since its discovery in 1951 (Ewen & Purcell 1951; Muller & Oort 1951). When the H I 21 cm line is optically thin, the following equation is used to calculate the H I column density, $N_{\text{H I}}$, from the 21 cm line intensity, $W_{\text{H I}}$,

$$N_{\text{H I}} (\text{cm}^{-2}) = 1.823 \times 10^{18} W_{\text{H I}} (\text{K km s}^{-1}). \quad (1)$$

As such, it has been commonly thought that 21 cm H I emission is optically thin. Direct support for the optically thin assumption for H I is obtained by the emission-absorption measurements toward radio continuum compact sources, which show that the H I peak optical depth is typically ~ 0.1 (e.g., Dickey et al. 2003; Heiles & Troland 2003a,b). High resolution H I observations with the Arecibo 305 m telescope have been used to make high sensitivity emission-absorption measurements and revolutionized the knowledge on the H I gas physical conditions (Heiles & Troland 2003b). In the meantime the question was raised that the 21 cm H I emission may be optically thick based on H I profiles with self-absorption (Braun 2012). Because H I observations provide physical quantities averaged along a line of sight, it is in principle impossible to retrieve the original physical parameters of the H I gas in the three dimensions, making it

difficult to test observationally the above H I properties for the large volume where H I is distributed.

The dust emission and extinction are also used often as a proxy for $N_{\text{H I}}$ under an assumption of constant gas to dust ratio. Previously, the scattering in the data for dust column density against $W_{\text{H I}}$ was large, making the method crude at best (see e.g., Chapter 21 of Draine 2011). Planck Collaboration (2014) opened a new possibility of precise measurement of dust optical depth by making extremely sensitive measurements of dust optical depth at sub-mm wavelengths, 350, 550 and 850 microns. These long wavelengths are in the Rayleigh-Jeans regime of the Planck function and, by combining with the *IRAS* data at 100 microns in the Wien regime, the sub-mm dust optical depth and dust temperature for an appropriate dust emissivity β were calculated with unprecedented accuracy to within 10%.

Fukui et al. (2014, 2015) presented a method to use the *Planck/IRAS* dust optical depth at 353 GHz (τ_{353}) as a proxy of $N_{\text{H I}}$ by identifying the optically thin regime of 21 cm H I emission as a linear part of a scatter plot between $W_{\text{H I}}$ and τ_{353} , where dispersion of the data points is smallest at the highest dust temperature. Fukui et al. (2014) presented results for high-latitude clouds with the Galactic Arecibo L-band Feed Array H I (GALFA-H I) survey data (Peek et al. 2011) taken with a 4' beam of the Arecibo telescope and Fukui et al. (2015) for the whole sky at $|b|$ larger than 15° with a 33' beam in the Leiden/Argentine/Bonn (LAB) survey (Kalberla et al. 2005). The two papers concluded that, in the local interstellar volume within 200 pc of the sun, interstellar H I is dominated by cold and dense H I gas which is optically thick with a typical H I optical depth of ~ 1 , and that the average H I density is to be doubled approximately if the correction for the optical depth is applied. Fukui et al. (2015) argued that the opacity-

corrected H I can explain the “dark gas”, which is detected in γ -rays and interstellar extinction A_V but not in the 2.6-mm CO or optically-thin 21-cm H I transitions (Grenier et al. 2005; Grenier et al. 2015 for a review), as an alternative to CO-free H₂ gas (Wolfire et al. 2010). In order to understand the behavior of H I, it is crucial to measure the fraction of H₂ in H I gas. Since H₂ has no radio transition, ultraviolet (UV) absorption of the electronic transition provides a unique tool to directly measure H₂. *FUSE* and *Copernicus* results are such datasets of H₂ (e.g., Gillmon et al. 2006). Since observations need background UV sources which are located at high b , the H₂ observations measure H₂ in the local interstellar medium close to the sun. We are able to use the H₂ data in modeling the local interstellar medium. In some cases H I can be measured as well in UV. Also, H I measurements at 21 cm in line absorption toward radio continuum sources provide H I column density (e.g., Heiles & Troland 2003a,b).

There remain two issues which were not addressed in Fukui et al. (2014, 2015). One is the contribution of the warm neutral medium (WNM). Pioneering studies by Field (1965) and Field et al. (1969) showed that the interstellar medium consists of the two phases, the CNM and the WNM, which are in pressure equilibrium. Because the dust grains are included in the both phases, the cold neutral medium (CNM) and WNM, the H I emission analyzed with the *Planck/IRAS* data should include the contribution of the WNM. The other is the possible effect of dust evolution found by Roy et al. (2013) which may require some modification of the linear relationship between N_{HI} and τ_{353} assumed by Fukui et al. (2014, 2015). H I emission-absorption measurements were used to constrain H I parameters of the CNM and WNM (Dickey et al. 2003; Heiles & Troland 2003a,b), where the WNM manifests itself as broad line wings of H I emission profiles.

There remains yet an uncertainty in deriving the WNM temperature in absorption, and only a lower limit for the spin temperature T_s was obtained to be around 500 K, leaving the mass of the WNM uncertain, which may occupy $\sim 60\%$ of total H I (Heiles & Troland 2003b). In addition, the spatial distribution of the CNM and the WNM is not clearly understood yet while the CNM is suggested to occupy smaller volume than the WNM (Field & Saslaw 1965).

Following Fukui et al. (2014, 2015), Stanimirović et al. (2014) made H I emission-absorption measurements toward radio continuum sources in Perseus with the Arecibo H I data and found that the absorption optical depth is not so large as suggested by Fukui et al. (2014, 2015), raising a question on the optically thick H I emission. Their results are consistent with those by Heiles & Troland (2003a,b). McKee et al. (2015) made a comparison of Fukui et al. (2015) with the H I model by Heiles et al. (1981) and discussed that the two results are consistent within $\sim 10\%$ in spite of their different H I optical depth. The reason for this agreement is not clarified. The method by Fukui et al. (2015) is based on a simple assumption of uniform interstellar medium and may need modification if realistic non-uniform physical properties of the interstellar medium are taken into account. The real H I observations are, however, limited because we are not able to assess the actual three dimensional physical conditions of the H I gas emitting/absorbing 21 cm line radiation.

A possible solution to overcome the difficulty and to test the above discrepancy is to utilize the results of hydrodynamical numerical simulations of the H I gas (Murray et al. 2015, 2016). Recently, three-dimensional hydrodynamical simulations modeled converging H I flows and achieved realistic density distributions and kinematics with high inhomogeneity and strong turbulence (Hennebelle et al.

2008; Heitsch et al. 2009; Banerjee et al. 2009; Vázquez-Semadeni et al. 2011; Inoue & Inutsuka 2012; Kim et al. 2014). These simulations are supported by observations of nearby galaxies which show turbulent H I gas with density of $10\text{--}100\text{ cm}^{-3}$ and molecular clouds formed from H I gas (Blitz & Rosolowsky 2006; Fukui et al. 1999, 2008, 2009; Kawamura et al. 2009; Fukui & Kawamura 2010).

In order to clarify the cause of the difference between the emission-absorption measurements of H I and the *Planck/IRAS*-based method of Fukui et al. (2014, 2015) and to have a better understanding of the CNM and the WNM, we examine synthetic H I line profiles by using the data of magneto-hydrodynamical (MHD) numerical simulations where the density, temperature, and velocity of the H I gas are available in three dimensions (Inoue & Inutsuka 2012). These simulations deal with converging H I flows as a function of time over 10 Myrs. The gas is originally H I, while formation of H₂ molecules is incorporated by using the usual dust surface reaction. The results indicate two phases of H I, the CNM and the WNM, as well as time-dependent transient gas which behaves intermediately. In the following we call for convenience the gas with T_s below 300 K the CNM and that with T_s above 300 K the WNM.

In the present paper we focus on the spatial distribution of the H I gas derived from the synthetic observations and explore the astrophysical implications of the emission-absorption measurements on the H I properties. Another paper which compares the synthetic observations and Fukui et al. (2014, 2015) will be published separately. The paper is organized as follows; Section 2 gives the results of the simulations, Section 3 presents results of synthetic observations with discussion and Section 4 describes the spatial distribution of the H I optical depth and column density with discussion. In Section 5 we present the conclusions.

2. RESULTS OF SIMULATIONS

2.1. Simulation Data and Model Selection

We summarize the relevant physical parameters and symbols in Table 1. We then give a brief explanation of the physical parameters and settings of the MHD simulations. More details are found in Inoue & Inutsuka (2012). The simulations assume converging H I gas flows at 20 km s^{-1} which are initially in pressure equilibrium with the standard interstellar H I having pressure of $pk_B^{-1} = 5.2 \times 10^3\text{ K cm}^{-3}$. The x -, y - and z -axes are taken as in Figure 2 of Inoue & Inutsuka (2012) and the flow direction is parallel to the x -axis. The H I gas flow is inhomogeneous and continuously enters into the box from the two opposite boundaries of a cube of $(20\text{ pc})^3$. In the interface of the converging flows turbulence is excited and the magnetic field is amplified. Formation of molecules such as H₂ formation on dust surfaces and CO formation via CH₂⁺ with the effects of self/dust UV shielding are taken into account and radiative and collisional heating and atomic and molecular cooling are incorporated. The simulation data are provided as the three dimensional data cube with 512^3 uniform pixels¹ and each pixel having a size of 0.04 pc in each axis with the physical parameters as listed in Table 2. The simulations are made over a timescale of 10 Myrs, ten times the typical crossing timescale of the local H I gas in the solar neighborhood. The total gas mass in the numerical domain increases with time. In order to extract the colliding gas for the present analysis, we excluded the gas injected prior to the collision in the simulation box. The spatial distribution of the colliding gas is localized around the central part of the box in the x -axis and is significantly different in its intensity from

¹ Inoue & Inutsuka (2012) made the simulations with dividing the numerical domain into 1024^3 pixels but the data were provided at a factor-of-two lower resolution to reduce the data size.

Table 1. Summary of symbols in the text

Symbol	Description
n_X	Number densities of atomic/molecular species, $X = \text{H I}, \text{H}_2$ etc.
τ_{353}	Dust optical depth at 353 GHz by Planck Collaboration (2014)
T_k	Kinetic temperature of gas
$\tau_{\text{H I}}, T_s$	H I optical depth and spin temperature
$\tau_{\text{H I}}^{\text{model}}$	Model H I optical depth given by Equation (6)
$\tau_{\text{H I}}^{\text{abs}}$	H I optical depth obtained by emission-absorption measurements (Eq. 15)
$\langle T_s \rangle$	Density-weighted harmonic mean of T_s along a line-of-sight (Eq. 16)
T_b	Brightness temperature of H I spectrum
$W_{\text{H I}}$	Velocity integrated-intensity of H I spectrum
$W_{\text{H I}}^{\text{WNM}}$	WNM integrated-intensity calculated by setting $\epsilon = 0$ of the CNM, while κ is held fixed
$W_{\text{H I}}^{\text{CNM}}$	CNM integrated-intensity defined by $W_{\text{H I}}^{\text{CNM}} = W_{\text{H I}} - W_{\text{H I}}^{\text{WNM}}$
$N_{\text{H I}}$	H I column density
$N_{\text{H I}}^{\text{model}}$	Model H I column density given by $\sum_j n_{\text{H I},j} \Delta y$
$N_{\text{H I}}^{\text{thin}}$	H I column density obtained under assumption of optically-thin H I line (Eq. 1)
$N_{\text{H I}}^{\text{HT}}$	Heiles & Troland (2003a) H I column density
f_{H_2}	Molecular fraction defined as $f_{\text{H}_2} = 2N_{\text{H}_2}/(2N_{\text{H}_2} + N_{\text{H I}})$ or $f_{\text{H}_2} = 2n_{\text{H}_2}/(2n_{\text{H}_2} + n_{\text{H I}})$
$M_{\text{H I}}$	Mass of H I
$M_{\text{H I}}^{\text{thin}}$	Mass of H I obtained from $N_{\text{H I}}^{\text{thin}}$

Table 2. Summary of the physical parameters in the MHD model

Symbol	Description
pk_B^{-1}	Thermal pressure of gas, $T_k = pk_B^{-1} (\sum_X n_X)^{-1}$
(V_x, V_y, V_z)	Velocity vector

the injected gas. In order to eliminate the injected gas we set a lower limit of the synthetic H I intensity (see section 2.3) at 150 K km s^{-1} in the projected x - z plane. Figure 1 illustrates the boundary determined in that way by red contours in the three dimensional view at an epoch of 0.5 Myrs.

Figures 2(a)–(d) show the distributions of the synthetic data points in the $(N_{\text{H I}} + 2N_{\text{H}_2})$ - f_{H_2} plane, where the integration was made for 10 pc along the y -axis. Data at the four time steps, 0.3, 0.5, 1 and 3 Myrs, are shown (see the physical parameters in Table 3). UV observations

of f_{H_2} toward extra-galactic sources ([Gillmon et al. 2006](#)) are shown by open circles in each panel and are summarized in Table 4, where the number of observed sources for f_{H_2} is limited to 19. We did not include Galactic OB stars which may be contaminated by localized gas ([Rachford et al. 2002](#)), possibly causing unreliable f_{H_2} values for the local ISM. The ranges of $N_{\text{H I}}$ and f_{H_2} are consistent with those of the synthetic data points, whereas the UV measurements are limited to $N_{\text{H}_2} < 10^{21} \text{ cm}^{-2}$. In order to choose the epoch of the model, we compared the measured distribution of f_{H_2} with the model.

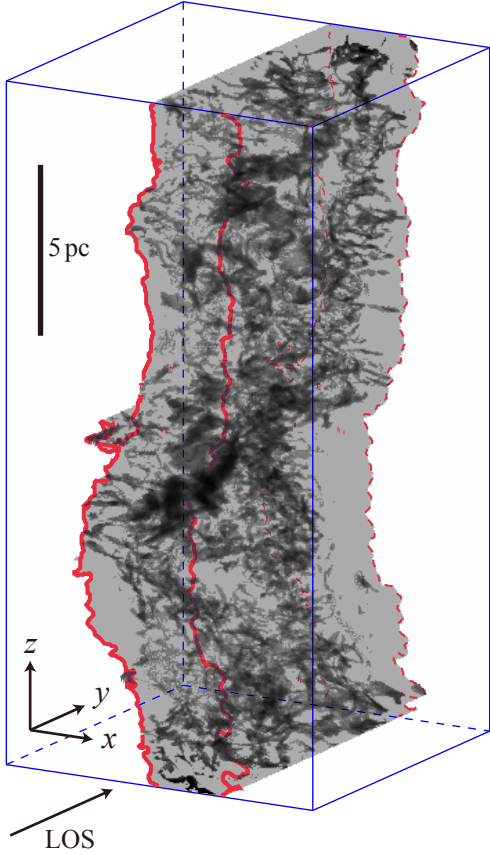


Figure 1. Volume rendering map of spatial distribution of pixels with $T_s < 300$ K (black) and those with $T_s > 300$ K (gray) in the 0.5-Myr model. The red contour projected on the front surface outlines the region of interest (ROI). The pixels out of the ROI are blanked and not used in Figures 2, 4(a), 5, 10, 11, 13, 15 and Table 3.

Figures 3(a)–(d) show the corresponding histograms of f_{H_2} in the model. Figure 4 shows a typical hydrogen column density distribution. The points of the UV measurements have total hydrogen column density less than 10^{21} cm^{-2} , and the comparison was made substantially at $N_{\text{H}_1} + 2N_{\text{H}_2}$ less than 10^{21} cm^{-2} . Figure 3 shows that f_{H_2} increases by the H_2 formation reaction in time, while the $N_{\text{H}_1} + 2N_{\text{H}_2}$ distribution does not change significantly among the epochs (Figure 2). By comparing Figures 3(a)–(d) with the histogram of the measured f_{H_2} in Figure 3(e), we found that the 0.5-Myr model shows the best presentation of the UV measurements in the av-

erage and dispersion of f_{H_2} . We shall use the 0.5-Myr model for the present analysis. Figure 4 gives histograms of total column density $N_{\text{H}_1} + 2N_{\text{H}_2}$ in the model and N_{H_1} of the observations by Fukui et al. (2015)². As seen in Table 3 the fraction of H_2 is negligibly small in the 0.5-Myr model.

2.2. HI distributions

Figures 5(a) and 5(b) shows histograms of density ($n = n_{\text{H}_1} + 2n_{\text{H}_2}$) and temperature (T_k) in the model. Figure 5(c) shows a probability distribution function in the density-temperature plane and indicates that temperature is roughly inversely proportional to density. We find that density and temperature have large ranges covering the CNM and WNM, whereas we do not see clear bimodal distribution corresponding to each of the CNM and WNM with a boundary at 300K in Figure 5 due to intermediate gas formed by the strong turbulent mixing in the model. Note that the typical ISM is affected by supernovae with every a few million years and duration of compression (or lifetime of a supernova shock) is about 1 million years. The ISM compressed by the converging flows in the 0.5–1.0 Myr seems to be the representative state of the dynamic ISM.

Three-dimensional distribution of the model is shown in Figure 1. The CNM and the WNM have distinctly different spatial distributions. The CNM is highly clumpy with size scales of a few pc to sub-pc, whereas the WNM is diffuse and smooth. The volumes of the CNM and the WNM are 3.5% and 96.5%, respectively. The CNM is dense gas which quickly cools down, and the WNM has high temperature and high pressure. These physical properties produce the different spatial distributions. It is not appro-

² Fukui et al. (2015) obtained H I column densities assuming a linear relationship $N_{\text{H}_1} \propto \tau_{353}$ but we obtained total column densities by applying a nonlinear relationship $N_{\text{H}_1} + 2N_{\text{H}_2} \propto \tau_{353}^{1/1.3}$ (Okamoto et al. 2017).

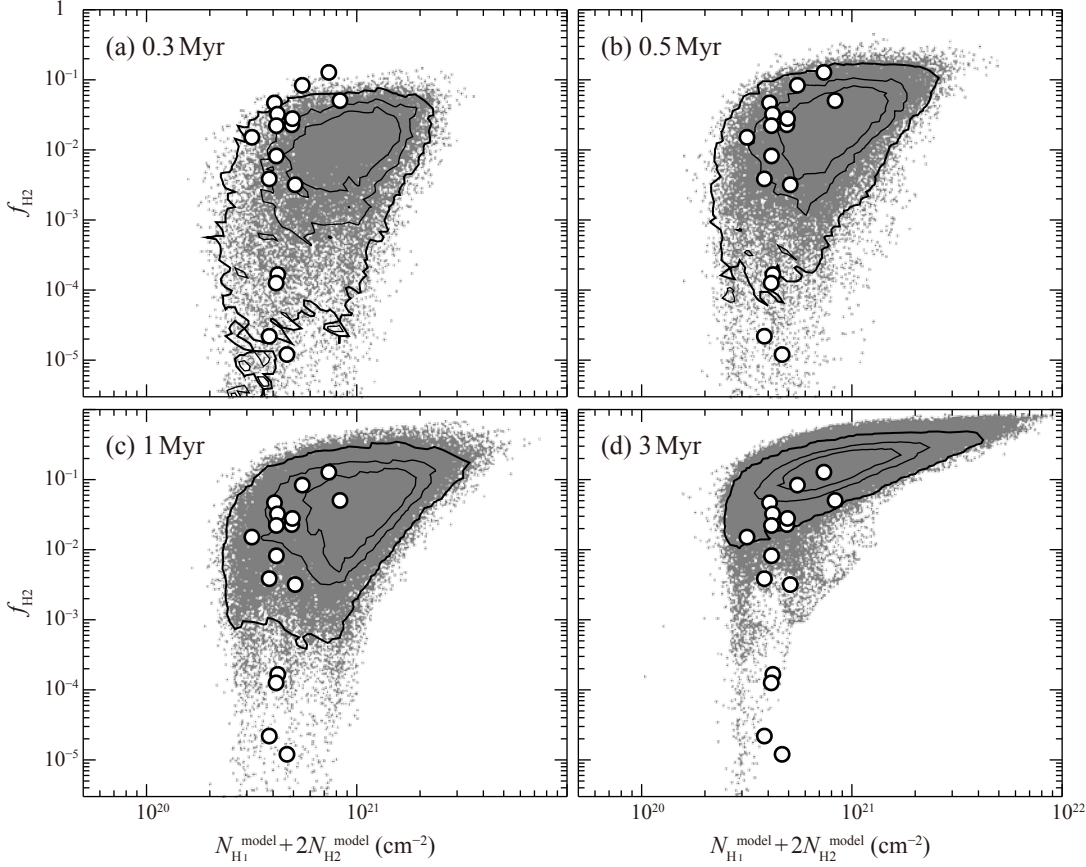


Figure 2. (a) Plot of molecular fraction defined as $f_{\text{H}_2} = 2N_{\text{H}_2}/(2N_{\text{H}_2} + N_{\text{H}_1})$ for total column density $N_{\text{H}_1} + 2N_{\text{H}_2}$ at a time step of 0.3 Myr. The contours includes 45%, 70% and 95% of data points. The open circles show the results of direct UV absorption measurements of H_2 by *FUSE* toward AGNi (summarized in Table 4, 3 out of 19 are not shown due to low $f_{\text{H}_2} \sim 10^{-6}$). (b)–(d) Same as (a) but at time steps of 0.5 Myr, 1 Myr, and 3 Myr, respectively.

appropriate to characterize the two media by representative density or temperature because they range over two to three orders of magnitude as seen in Figure 5. $T_k = 300$ K as a boundary between the CNM and WNM is consistent with a typical $T_k \sim 70$ K of the CNM and a typical T_k range of the WNM 500 K–5000 K (Heiles & Troland 2003b). The masses of the CNM and WNM are $150 M_\odot$ and $244 M_\odot$, respectively in the present model. The CNM and WNM are far from the dynamical equilibrium which was discussed in a classical picture of the ISM (Field 1965), but are highly transient and time-dependent (cf. Figure 5(c)). The time scale of the ISM evolution is in the order of Myr as estimated by a ratio of 10 km s^{-1} divided by 10 pc .

This is comparable to that of the shock front passage driven by SNRs and is supposed to be usual as the ISM in the solar neighborhood (Inoue & Inutsuka 2012).

2.3. Synthetic observations of H I Line Profiles

2.3.1. Density distribution in a line of sight

Figure 6(a) gives a side view of the density profile of the model in the y - z plane integrated in the x -direction. In order to show typical line profiles, we chose three lines of sight P, Q and R which have similar total 21 cm line intensity W_{H_1} with different column density N_{H_1} . Panels (b)–(d) of Figure 6 show distributions of density and temperature for each pixel in the three lines of sight P, Q, and R. The CNM appears

Table 3. Physical parameters from the models at different time steps

Time step (Myr)	M_{HI} (M_{\odot})	$M_{\text{HI}}^{\text{thin}}$ (M_{\odot})	$\frac{M_{\text{HI}}}{M_{\text{HI}}^{\text{thin}}}$ (4)	M_{H2} (M_{\odot})	$\frac{M_{\text{H2}}}{M_{\text{H2}}+M_{\text{HI}}}$ (6)	$\frac{M_{\text{CNM}}}{M_{\text{HI}}}$ (7)	$\frac{M_{\text{WNM}}}{M_{\text{HI}}}$ (8)	CNM volume filling factor (9)	CNM covering factor (10)
(1)	(2)	(3)	(4)	(5)	(6)	(7)	(8)	(9)	(10)
0.3	265	205	1.3	4.5	1.7×10^{-2}	0.39	0.61	3.4%	30.4%
0.5	394	309	1.3	18.8	4.6×10^{-2}	0.38	0.62	3.5%	28.5%
1.0	745	563	1.3	74.6	9.1×10^{-2}	0.39	0.61	5.0%	35.7%
3.0	1731	1114	1.6	660.5	2.8×10^{-1}	0.60	0.40	12.6%	50.6%

NOTE— Columns (2): mass of H I gas, (3): mass of H I given from H I integrated-intensity under the optically-thin assumption, (4): ratio of (2) to (3), (5): mass of H₂ gas, (6): mass fraction of H₂ gas, (7): ratio of CNM mass to (2), (8): ratio of WNM mass to (2), (9): volume filling factor of the CNM, (10): projected area covering factor of the CNM with $\int \tau_{\text{HI}}^{\text{model}}(V)dV > 4 \text{ km s}^{-1}$ (see sections 3 and 4.1).

as a few spikes with a sub-pc size whose typical density is 10^2 to 10^3 cm^{-3} . The WNM is distributed with density less than 100 cm^{-3} and show smooth distribution.

The distributions of various H I physical parameters which are required in calculating line profiles are given in Figure 7 for the line of sight P. Figure 7(i) shows n and T_s , Figure 7(ii) line of sight velocity V_y , and Figure 7(iii) the maximum opacity and the optical depth. The opacity is integrated in the line of sight to yield optical depth. The accumulated optical depth reaches ~ 1 and is determined by a few CNM spikes in each line of sight as seen in Figure 7(iii). The WNM has little contribution to the optical depth, which is a natural consequence of the T_s^{-1} -dependence of opacity (see Equation (5)).

2.3.2. Calculations of H I Line Profiles

The simulated ISM is used to calculate synthetic H I profiles by using the line radiation transfer equation given as

$$I_{j+1}(V) = I_j(V) \exp[-\kappa_j(V)\Delta y] + \frac{\epsilon_j(V)}{\kappa_j(V)} \{1 - \exp[-\kappa_j(V)\Delta y]\} \quad (2)$$

$$I_0 = B(T_{\text{bg}}) \sim \frac{2\nu_0^2}{c^2} k_B T_{\text{bg}}, \quad (3)$$

$$n_{\text{low},j} = \frac{n_{\text{HI},j}}{3 \exp\left(\frac{-h\nu_0}{k_B T_{s,j}}\right) + 1} \quad (7)$$

where $I(V)$ the line intensity, $\kappa(V)$ opacity, $\epsilon(V)$ emissivity, $B(T)$ the Planck function at 21 cm, $\nu_0 = 1.420405751 \text{ GHz}$, $T_{\text{bg}} = 2.7 \text{ K}$ the brightness temperature of the background radiation field, c the light velocity and k_B Boltzmann constant. The subscript j stands for the j -th cell along a line of sight. The emissivity ϵ and opacity κ of the 21 cm transition at a radial velocity V are calculated as follows;

$$\epsilon_j(V) = \frac{hc}{4\pi} n_{\text{up},j} A \phi_j(V), \quad (4)$$

$$\kappa_j(V) = \frac{3c^3 h}{8\pi\nu_0^2 k_B T_{s,j}} n_{\text{low},j} A \phi_j(V), \quad (5)$$

where h and $A = 2.8688754 \times 10^{-15} \text{ s}^{-1}$ are the Planck constant and the Einstein A coefficient, respectively. The H I optical depth at a radial velocity V , $\tau_{\text{HI}}(V)$, obtained by integration in a line of sight is calculated as follows;

$$\tau_{\text{HI}}(V) = \sum_j [\kappa_j(V)\Delta y]. \quad (6)$$

The number density of H atom in the lower state is given by

Table 4. Targets of the f_{H_2} estimates

Target	l	b	N_{H_2} (cm^{-2})	τ_{353}	$N_{\text{H}_1} + 2N_{\text{H}_2}$ (cm^{-2})	f_{H_2}
(1)	(2)	(3)	(4)	(5)	(6)	(7)
3C 249.1	130°39	+38°55	9.5×10^{18}	2.51×10^{-6}	4.1×10^{20}	4.7×10^{-2}
ESO 141–G55	338°18	–26°71	2.1×10^{19}	6.38×10^{-6}	8.3×10^{20}	5.0×10^{-2}
H1821+643	94°00	+27°42	8.1×10^{17}	3.37×10^{-6}	5.1×10^{20}	3.2×10^{-3}
HE 1143–1810	281°85	+41°71	3.5×10^{16}	2.63×10^{-6}	4.2×10^{20}	1.7×10^{-4}
MRC 2251–178	46°20	–61°33	3.5×10^{14}	1.23×10^{-6}	2.3×10^{20}	3.0×10^{-6}
Mrk 9	158°36	+28°75	2.3×10^{19}	3.73×10^{-6}	5.5×10^{20}	8.4×10^{-2}
Mrk 335	108°76	–41°42	6.8×10^{18}	2.62×10^{-6}	4.2×10^{20}	3.2×10^{-2}
Mrk 509	35°97	–29°86	7.4×10^{17}	2.33×10^{-6}	3.8×10^{20}	3.9×10^{-3}
Mrk 1383	349°22	+55°12	2.2×10^{14}	1.55×10^{-6}	2.8×10^{20}	1.6×10^{-6}
Mrk 1513	63°67	–29°07	2.6×10^{16}	2.57×10^{-6}	4.1×10^{20}	1.3×10^{-4}
MS 0700.7+6338	152°47	+25°63	5.6×10^{18}	3.21×10^{-6}	4.9×10^{20}	2.3×10^{-2}
NGC 7469	83°10	–45°47	4.7×10^{19}	5.44×10^{-6}	7.4×10^{20}	1.3×10^{-1}
PG 0804+761	138°28	+31°03	4.6×10^{18}	2.58×10^{-6}	4.1×10^{20}	2.2×10^{-2}
PG 0844+349	188°56	+37°97	1.7×10^{18}	2.58×10^{-6}	4.1×10^{20}	8.2×10^{-3}
PG 1211+143	267°55	+74°32	2.4×10^{18}	1.82×10^{-6}	3.2×10^{20}	1.5×10^{-2}
PG 1302–102	308°59	+52°16	4.2×10^{15}	2.33×10^{-6}	3.8×10^{20}	2.2×10^{-5}
PKS 0558–504	257°96	–28°57	2.8×10^{15}	3.00×10^{-6}	4.7×10^{20}	1.2×10^{-5}
PKS 2155–304	17°73	–52°25	1.5×10^{14}	7.92×10^{-7}	1.7×10^{20}	1.8×10^{-6}
VII Zw 118	151°36	+25°99	6.9×10^{18}	3.24×10^{-6}	4.9×10^{20}	2.8×10^{-2}

NOTE— Columns (1): name of target, (2) and (3): position in the Galactic coordinates, (4): H_2 column density derived with the UV measurements (Gillmon et al. 2006), (5): dust optical depth at 353 GHz (Planck Collaboration 2014), (6): total column density obtained from τ_{353} by taking into account a nonlinear relationship (Okamoto et al. 2017), (7): H_2 fraction given by $f_{\text{H}_2} = 2N_{\text{H}_2}/(2N_{\text{H}_2} + N_{\text{H}_1})$.

and that in the upper state is

$$n_{\text{up},j} = n_{\text{H I},j} - n_{\text{low},j} \quad (8)$$

for total H I density $n_{\text{H I}}$. The line shape function

$$\phi_j(V) = \sqrt{\frac{m_p + m_e}{2k_B T_{s,j} \pi}} \exp \left[\frac{-(m_p + m_e)(V - V_{y,j})^2}{2k_B T_{s,j}} \right] \quad (9)$$

satisfies $\int \phi(V) dV = 1$, where $m_p = 1.67262178 \times 10^{-24}$ g is the mass of a proton and $m_e =$

$9.10938291 \times 10^{-28}$ g is that of an electron. The H I spin temperature T_s is derived by applying a method of Kim et al. (2014), which gives $T_s \sim T_k$ in a T_k range from 20 to 3×10^3 K. For $T_k < 20$ K, we simply adopt $T_s = T_k$. The $\sim 75\%$ of the data pixels have $T_s/T_k = 0.9$ –1.0 and the others $T_s/T_k = 0.8$ –0.9.

2.3.3. Emission profiles

An H I line profile is calculated by integrating the line transfer Equations (2) and (3) from the far side to the near side of the data cube

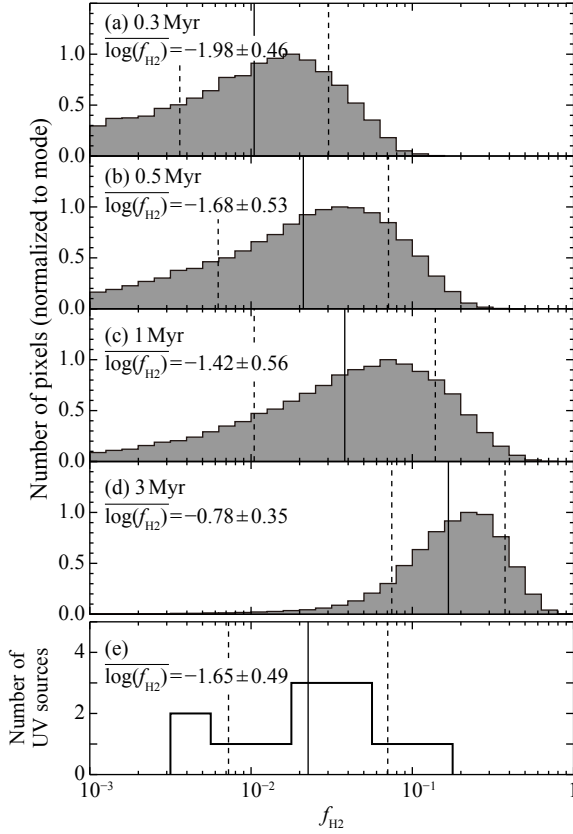


Figure 3. Histograms of f_{H_2} in the models at four epochs at 0.3 Myrs, 0.5 Myrs, 1 Myrs and 3 Myrs. Panel (a) presents the 0.3-Myr model. The average and dispersion (1σ) of f_{H_2} are shown as corresponding bars with of a solid line and two dashed lines, respectively. Panels (b)–(d) show similar plots at the other epochs. Panel (e) shows a histogram of f_{H_2} by the UV measurements listed in Table 4, and presents the same quantities as above.

along the y -axis seen by the observer over a distance of 10 pc, a half of the full span of the data cube, and the observed brightness temperature is given by

$$T_b(V) = I(V) \frac{c^2}{2\nu_0^2 k_B} - T_{\text{bg}}, \quad (10)$$

which is approximated for convenience as

$$T_b(V) = [T_s(V) - T_{\text{bg}}] \{1 - \exp[-\tau_{\text{H I}}(V)]\}, \quad (11)$$

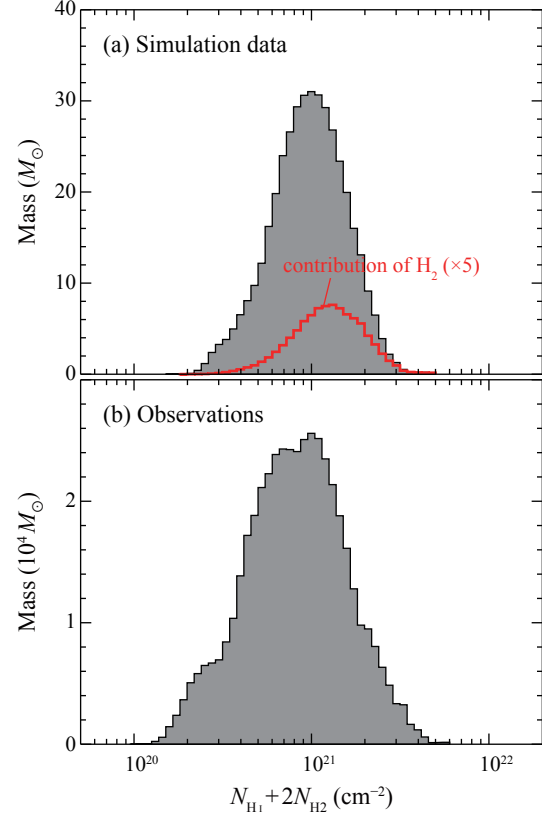


Figure 4. (a) Mass histograms of total column density, $N_{\text{H I}} + 2N_{\text{H}_2}$ in the 0.5-Myr model. The red line represents the contribution of H_2 (multiplied by a factor of 5). (b) Same as (a) but for the observational dataset used in Fukui et al. (2015). Here the total column densities are given from τ_{353} (Planck Collaboration 2014) by taking into account a nonlinear relationship.

where T_s is a harmonic mean spin temperature in a line of sight,

$$\frac{\sum_j [n_{\text{H I},j} \phi_j(V)]}{T_s(V)} = \sum_j \left[\frac{n_{\text{H I},j} \phi_j(V)}{T_{s,j}} \right] \quad (12)$$

and T_{bg} is subtracted as in real observations.

Figure 8(a) shows three emission line profiles; the black solid line is the emission of the whole H I gas, and the short-dashed- and long-dashed-lines give the emission from the warm gas with T_s higher than 300 K and 1000 K, respectively. $T_s > 1000$ K is shown for reference. The profiles only from the warm gas are calculated by setting the emissivity ϵ of the cold gas equal to 0, while

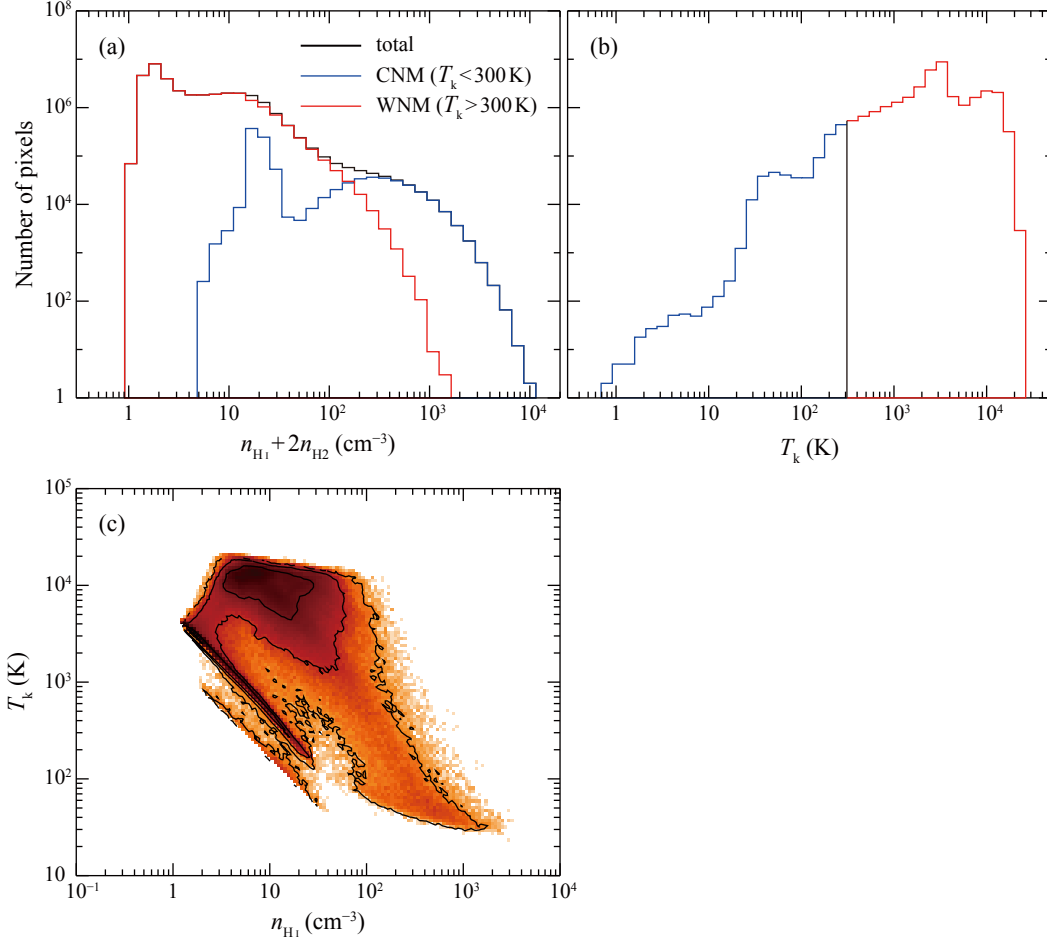


Figure 5. Histograms of (a) total hydrogen density ($n_{\text{H I}} + 2n_{\text{H}_2}$) and (b) kinetic temperature (T_{k}) for each pixel in the 0.5-Myr model. The blue lines represent the contribution of $T_{\text{K}} < 300$ K and red lines represent that of $T_{\text{K}} > 300$ K. (c) Probability distribution function in the $n_{\text{H I}}-T_{\text{k}}$ plane. The contours have equal logarithmic spacing. The straight distribution in the lower right shows the initial H I flows prior to the collision.

the opacity κ of the whole gas is fixed. It is seen that a T_{s} value is not so critical in discriminating the CNM and WNM.

Figure 8(a)-P shows an H I emission profile calculated for the line of sight P in Figure 5 for $4'$ resolution, the same with the Arecibo telescope. The intensity integrated over velocity gives the total intensity of a 21 cm line emission profile $W_{\text{H I}}$. The CNM has a narrow profile whose linewidth is $\sim 5 \text{ km s}^{-1}$, while the WNM shows a broad wing-like profile of $\sim 40 \text{ km s}^{-1}$ velocity span. The profiles are consistent with the observed one in the solar neighborhood (see the H I profiles at high b , e.g., Kalberla et al.

2005; Fukui et al. 2014, 2015). The model allows us to separate the contributions of the CNM and WNM, which is impossible in real observations. Figures 8(a)-Q and 8(a)-R show similar profiles in Q and R. Table 5 lists the derived physical parameters of the H I gas.

2.3.4. Emission-absorption profiles and H I column density

The emission-absorption method uses absorption on a radio continuum source and averaged emission profiles off the continuum source by assuming that the H I emission profiles are not significantly different between the two positions. An H I emission profile is a function of two

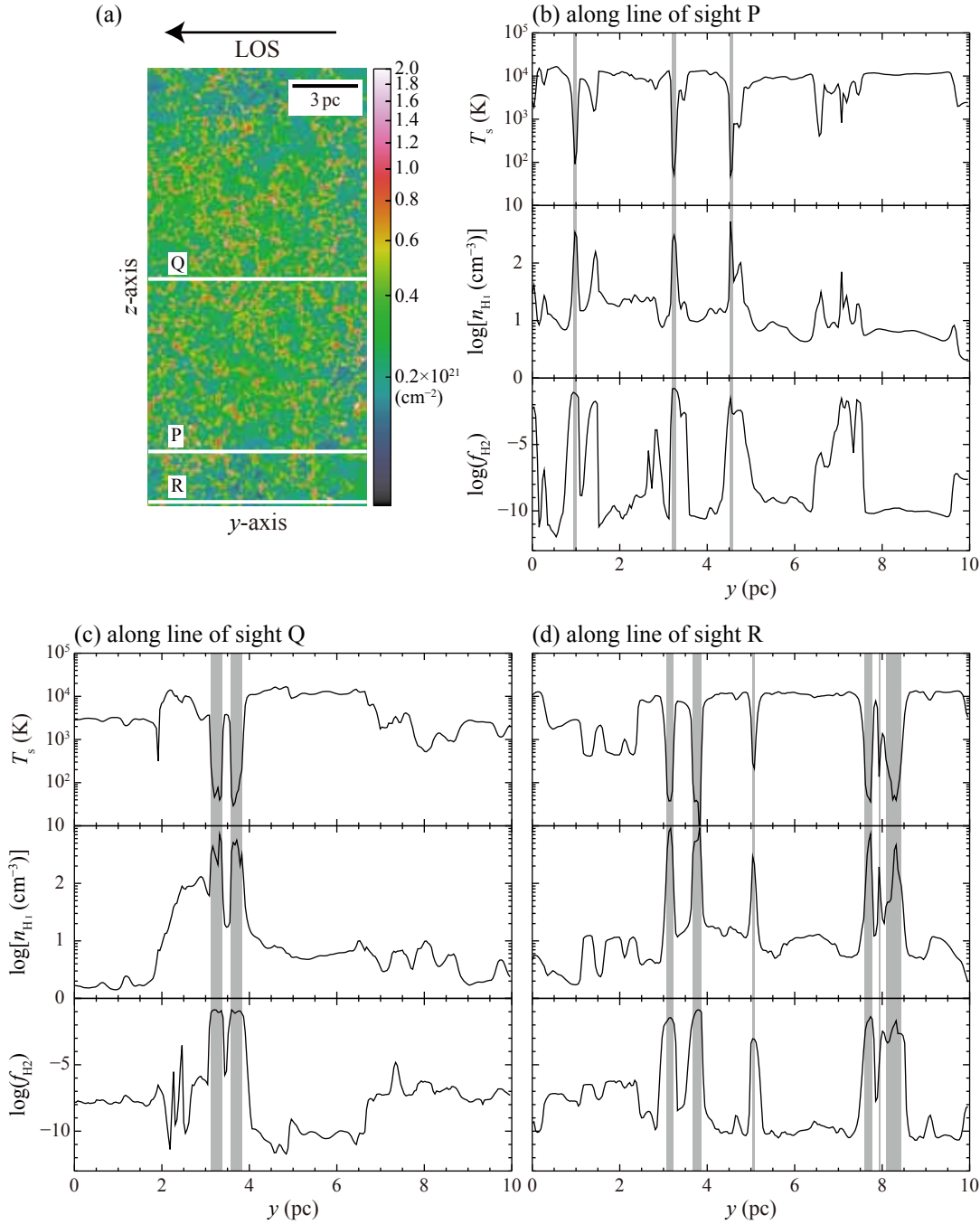


Figure 6. (a) Side view of the H I column density in the y - z plane integrated in the x -direction in the model. Three lines of sight selected are shown by the lines P, Q and R (see the text and Table 5). The image is $10 \text{ pc} \times 20 \text{ pc}$ in size. The y axis in the numerical domain corresponds to the horizontal axis and the z axis to the vertical axis. (b) T_s , $n_{\text{H I}}$ and H_2 fraction $f_{\text{H}_2} = 2n_{\text{H}_2}/(2n_{\text{H}_2} + n_{\text{H I}})$ profiles (from top to bottom) along the line of sight P. The horizontal axis is the distance from the far-side of the model ISM, y . The CNM spikes are indicated by shaded regions. (c) and (d) Same as (b) but along lines of sight Q and R, respectively.

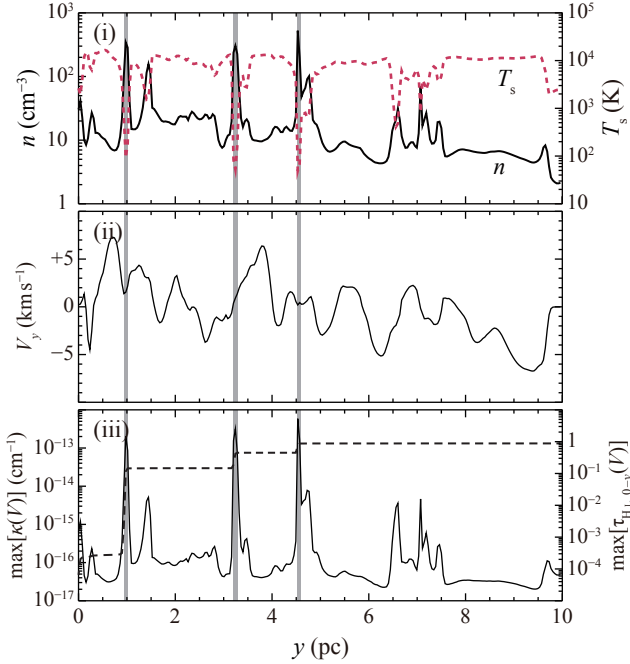


Figure 7. (i) Profiles of density (the solid black line) and spin temperature (the dashed red line) along the line of sight P. The horizontal axis is the distance from the far-side of the model ISM, y . Profiles of (ii) line-of-sight velocity, V_y , and (iii) peak opacity, $\max[\kappa(V)]$ given by Equation (5), along the same line of sight as (i) are shown. Peak optical depth $\max[\tau_{\text{H I}, 0-y}(V)] = \max[\int_0^y \kappa(V) dy']$ is plotted against right-side vertical-axis of panel (iii) by the dashed line. The CNM spikes are indicated by shaded regions.

unknowns, $T_s(V)$ and $\tau_{\text{H I}}(V)$, for a single observed quantity $T_b(V)$, and cannot be solved for $T_s(V)$ and $\tau_{\text{H I}}(V)$. By observing a radio continuum source as a background source, a second equation which relates $T_s(V)$ and $\tau_{\text{H I}}(V)$ is obtained, and the two equations are coupled to derive $T_s(V)$ and $\tau_{\text{H I}}(V)$ (e.g., [Draine 2011](#)).

The off-source brightness temperature $T_{b,\text{off}}$ and on-source brightness temperature $T_{b,\text{on}}$ are given as follows;

$$T_{b,\text{off}}(V) = [T_s(V) - 2.7 \text{ K}] \{1 - \exp[-\tau_{\text{H I}}(V)]\}, \quad (13)$$

and

$$T_{b,\text{on}}(V) = [T_s(V) - T_{\text{cont}}] \{1 - \exp[-\tau_{\text{H I}}(V)]\}. \quad (14)$$

Here T_{cont} is the temperature of an assumed background compact continuum source. The absorption spectra obtained from the emission-absorption measurements are given as,

$$1 - \exp[-\tau_{\text{H I}}^{\text{abs}}(V)] = \frac{T_{b,\text{off}}(V) - T_{b,\text{on}}(V)}{T_{\text{cont}} - 2.7 \text{ K}}. \quad (15)$$

Figure 8(b)-P shows $T_{b,\text{off}}(V)$ in Equation (13) (solid line) and $T_{b,\text{on}}(V)$ in Equation (14) (dashed line) toward a radio continuum compact source at P for $4'$ resolution and Figure 8(c)-P shows $1 - \exp[-\tau_{\text{H I}}^{\text{abs}}(V)]$ in Equation (15). The angular size of the radio continuum source is assumed to be equivalent to the pixel size $0.9''$, which is nearly consistent with the typical size of the radio continuum sources $20''$ – $30''$. In the real emission-absorption measurements the off-source spectrum is taken with a larger beam than the size of the radio continuum compact source. Figures 8(a)–(c)-Q and 8(a)–(c)-R are the same profiles for the directions Q and R.

In real observations an average of profiles near the on source position is used as $T_{b,\text{off}}$ (e.g., [Heiles & Troland 2003a](#)). In the synthetic observations we use the on-source emission profile by assuming a model background continuum source with a flux density of 1 Jy. As readily confirmed $\tau_{\text{H I}}^{\text{abs}}(V)$ is equal to $\tau_{\text{H I}}^{\text{model}}(V) = \int \kappa(V) dy$ integrated in the line of sight.

3. OBSERVED PROPERTIES OF THE H I GAS

Synthetic observations provide total H I 21 cm line intensity $W_{\text{H I}}$. Other parameters obtained include the H I column density $N_{\text{H I}}$, and the H I optical depth $\tau_{\text{H I}}$. We calculated these H I parameters for the CNM and the WNM separately. The projected distributions of $W_{\text{H I}}$, $N_{\text{H I}}^{\text{model}}$ and velocity-integrated $\tau_{\text{H I}}^{\text{model}}$, $\int \tau_{\text{H I}}^{\text{model}}(V) dV$ are shown in the nine panels of Figures 9(a)–(i). We note significant difference between the CNM and the WNM. The CNM is

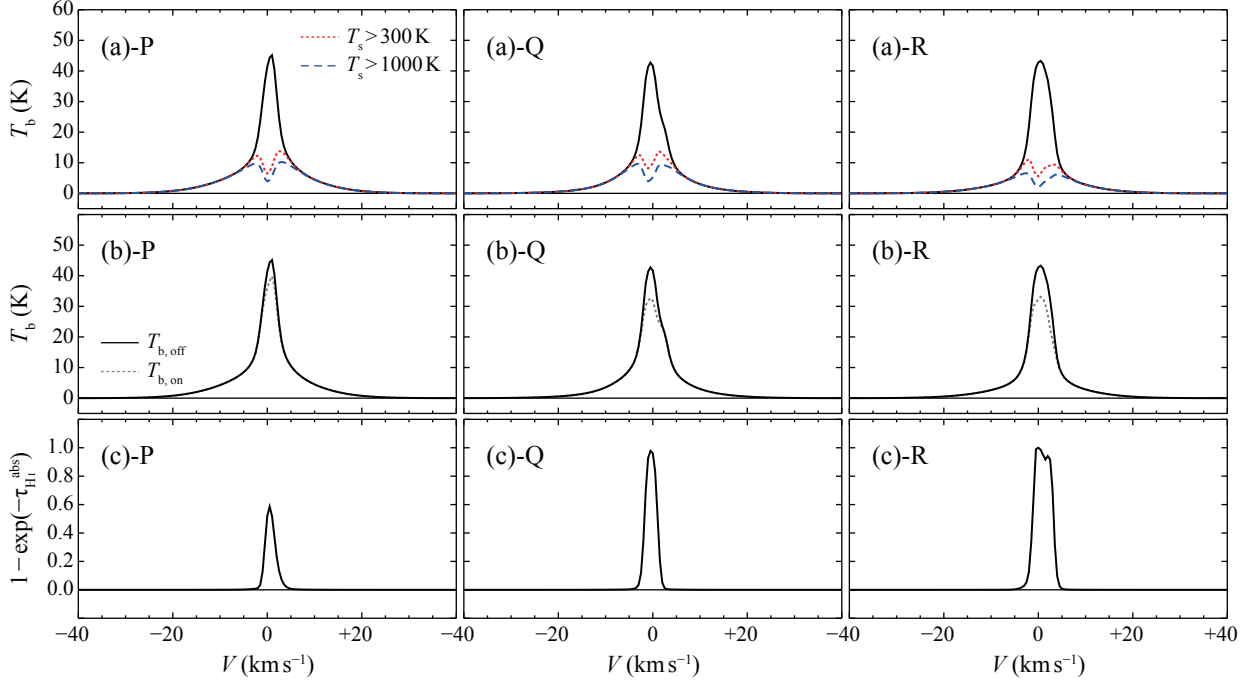


Figure 8. (a) Synthetic-observed H I emission spectra toward the different three directions. The solid lines are the emission of the whole H I gas, and the short-dashed- and long-dashed-lines give the emission from the warm gas with T_s higher than 300 K and 1000 K, respectively. The profiles only from the warm gas are calculated by setting the emissivity ϵ of the cold gas equal to 0, while the opacity κ of the whole gas is held fixed. (b) Synthetic-observed H I emission spectra. The solid lines show $T_{b,\text{off}}$ (Equation (13)) and the gray dashed lines show $T_{b,\text{on}}$ (Equation (14)). Here we assume a model background continuum source with a flux of 1 Jy. (c) Absorption spectra given by Equation (15).

highly filamentary and the WNM shows smooth distribution in the three parameters.

Figure 10 shows three histograms of W_{HI} , $N_{\text{HI}}^{\text{model}}$ and $\int \tau_{\text{HI}}^{\text{model}}(V)dV$ for the CNM and the WNM, respectively. A clear trend is that $N_{\text{HI}}^{\text{model}}$ is nearly comparable between the CNM and the WNM (Figure 10(b)). $\int \tau_{\text{HI}}^{\text{model}}(V)dV$ is dominated exclusively by the optically thick CNM (Figure 10(c)). These properties are shown numerically in Table 5. Table 5 shows details of the H I parameters including W_{HI} , N_{HI} , T_s , and $\int \tau_{\text{HI}}^{\text{model}}dV$ for representative three line profiles, which have similar W_{HI} . $N_{\text{HI}}^{\text{model}}$ is the integrated column density of the model and $N_{\text{HI}}^{\text{thin}}$ is calculated from W_{HI} by Equation (1). $W_{\text{HI}}^{\text{WNM}}$ is larger than the $W_{\text{HI}}^{\text{CNM}}$ at lower N_{HI} , while $W_{\text{HI}}^{\text{CNM}}$ becomes comparable to $W_{\text{HI}}^{\text{WNM}}$ at higher N_{HI} . $W_{\text{HI}}^{\text{WNM}}$ becomes large because T_s is high, in spite of the small $\int \tau_{\text{HI}}(V)dV$. The CNM is

usually optically thick with $\int \tau_{\text{HI}}(V)dV$ larger than ~ 2 , while the WNM is always optically thin. This large optical depth of the CNM make the ratio $N_{\text{HI}}^{\text{model}}/N_{\text{HI}}^{\text{thin}}$ larger than 1.0 at higher $\int \tau_{\text{HI}}(V)dV$. The WNM shows similar $N_{\text{HI}}^{\text{model}}$ and $N_{\text{HI}}^{\text{thin}}$, while $N_{\text{HI}}^{\text{thin}}$ is by a factor of 1.1–1.2 smaller than $N_{\text{HI}}^{\text{model}}$. This is due the absorption by the CNM. $\langle T_s \rangle$ represents a density-weighted harmonic mean of T_s in the line of sight expressed as follows;

$$\frac{\sum_j (n_{\text{HI},j})}{\langle T_s \rangle} = \sum_j \left(\frac{n_{\text{HI},j}}{T_{s,j}} \right). \quad (16)$$

Equation (16) reflects that $\int \tau_{\text{HI}}(V)dV$ is the sum of the contribution of different T_s components in the line of sight. $\langle T_s \rangle$ is calculated for the CNM and WNM, respectively, as well as for the whole profile. We note that the velocity averaged T_s in Fukui et al. (2014, 2015) corre-

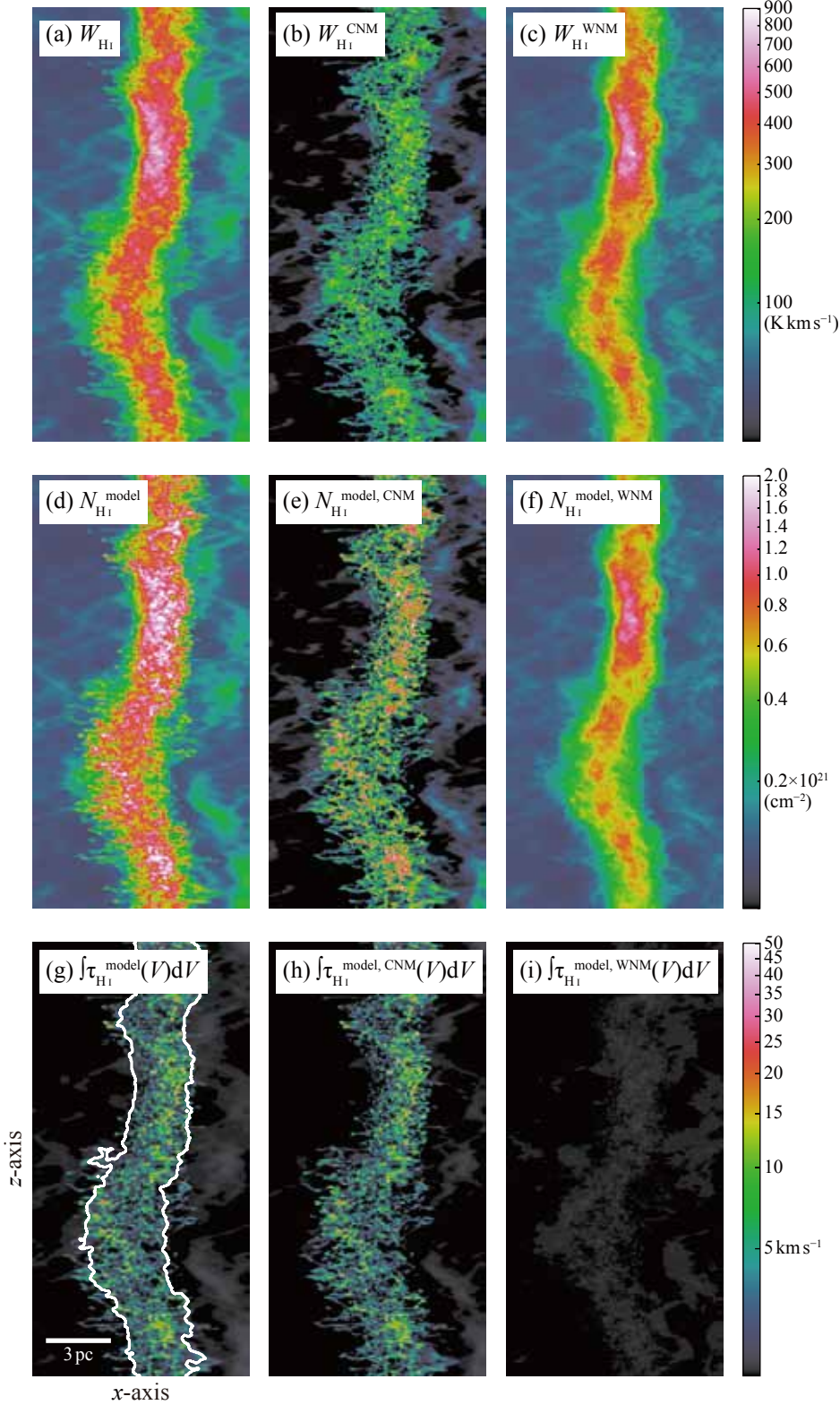


Figure 9. Spatial distribution of the 0.5-Myr model, (a) velocity-integrated intensity of the synthetic-observed H I spectra ($W_{\text{H I}}$), (b) $W_{\text{H I}}$ produced from the CNM with $T_{\text{k}} < 300 \text{ K}$, (c) $W_{\text{H I}}$ produced from the WNM with $T_{\text{k}} > 300 \text{ K}$, (d) model H I column density ($N_{\text{H I}}^{\text{model}}$), (e) CNM column density, (f) WNM column density, (g) velocity-integrated model optical depth ($\int \tau_{\text{H I}}^{\text{model}}(V) dV$), (h) those produced from the CNM and (i) produced from the WNM in the 0.5-Myr model. The images are $10 \text{ pc} \times 20 \text{ pc}$ in size and have a resolution of 0.04 pc per pixel. The x axis in the numerical domain corresponds to the horizontal axis of each panel and the z axis to the vertical axis. The contour in panel (g) outlines the ROI (identical to that shown in Figure 1).

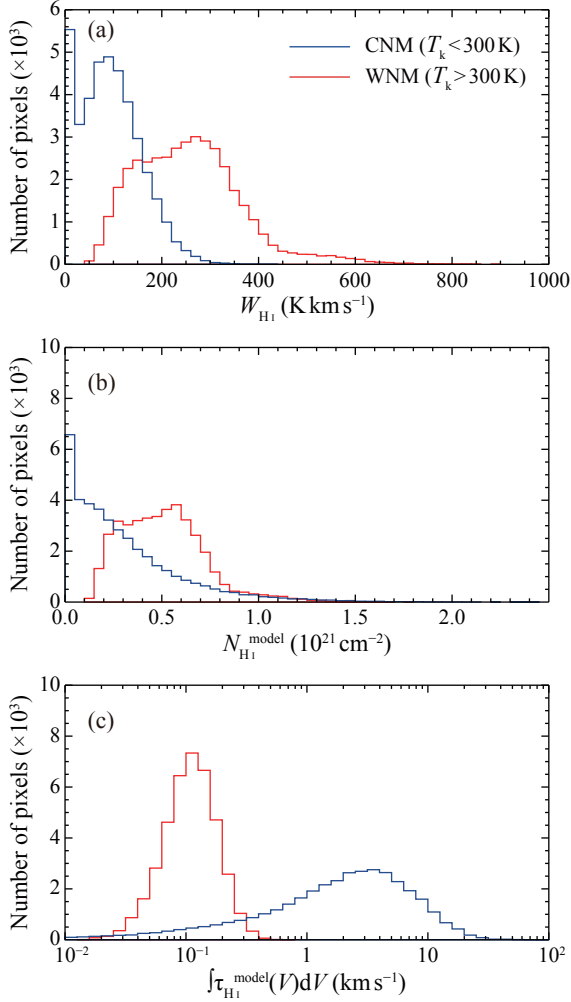


Figure 10. Histograms of (a) W_{HI} , (b) $N_{\text{HI}}^{\text{model}}$ and (c) $\int \tau_{\text{HI}}^{\text{model}}(V)dV$ in the 0.5-Myr model. The blue lines represent the contribution of the CNM and red lines represent that of the WNM.

sponds to $\langle T_s \rangle$ for the whole in the present notation. It is notable that the WNM shows practically no contribution to $\tau_{\text{HI}}^{\text{model}}$ (Figure 10(c)).

Figure 11(a) show a scatter plot between W_{HI} and $N_{\text{HI}}^{\text{model}}$, where $\langle T_s \rangle$ is indicated in a color code and $N_{\text{HI}}^{\text{model}}/N_{\text{HI}}^{\text{thin}} = 1.3$ by the dashed line. At $\langle T_s \rangle$ higher than 200 K, the optically thin approximation produces a linear relationship between W_{HI} and $N_{\text{HI}}^{\text{model}}$ as expressed by Equation (1), whereas at $\langle T_s \rangle$ lower than 100 K the H I optical depth becomes larger and W_{HI} becomes weaker than the thin limit due to saturation. This is consistent with the opti-

cally thick H I derived from the *Planck/IRAS*-based analysis by Fukui et al. (2015). Figure 11(b) shows $\int \tau_{\text{HI}}^{\text{model}}(V)dV$ as a function of $N_{\text{HI}}^{\text{model}}$. The median solid curve indicates that $\int \tau_{\text{HI}}^{\text{model}}(V)dV$ increases rapidly with $N_{\text{HI}}^{\text{model}}$ like $(N_{\text{HI}}^{\text{model}})^2$. This is explained by the relationship $\tau_{\text{HI}} = \text{constant} \times N_{\text{HI}}/(T_s \Delta V)$ (see Equation 15) where T_s is proportional to n^{-1} (Figure 5(c)) if ΔV remains fixed.

4. DISCUSSION; H I FILAMENTARY DISTRIBUTION AND ITS IMPACT ON THE EMISSION-ABSORPTION MEASUREMENTS

4.1. The CNM Filaments Observed in the Emission-Absorption Measurements

Figures 12(a) and 12(b) show detailed enlarged distributions of $N_{\text{HI}}^{\text{model}}$ and $\int \tau_{\text{HI}}^{\text{model}}(V)dV$, respectively. Because of the non-linear behavior of $\int \tau_{\text{HI}}(V)dV$, which is dominated by the CNM (Figure 11(b)), $\int \tau_{\text{HI}}(V)dV$ enhances the filamentary CNM distribution. The typical width of the filaments is less than 0.1 pc with their length of roughly 0.5 pc or more. It is conceivable that the small scale structures of $\int \tau_{\text{HI}}(V)dV$ significantly affect high resolution observations, and we explore the resolution effects in H I observations below.

4.1.1. Observed values of τ_{HI}

Figure 13 shows a histogram of $\int \tau_{\text{HI}}^{\text{model}}(V)dV$ at pixel-sized resolution of the spatial distribution presented in Figure 9(g). $\int \tau_{\text{HI}}^{\text{model}}(V)dV$ is distributed over a wide range from $2.5 \times 10^{-2} \text{ km s}^{-1}$ to $\sim 25 \text{ km s}^{-1}$ at a 5% level of the histogram, and from $6 \times 10^{-2} \text{ km s}^{-1}$ to 16 km s^{-1} at a 20% level. We also note that the small $\int \tau_{\text{HI}}^{\text{model}}(V)dV$ tail in $\int \tau_{\text{HI}}^{\text{model}}(V)dV$ below 1 km s^{-1} is significant, reflecting the wide spread WNM with low τ_{HI} . Conversely, high τ_{HI} points at $\int \tau_{\text{HI}}^{\text{model}}(V)dV$ more than 4 km s^{-1} is dominated by the compact CNM.

Pixel-sized resolution measurements are carried out in the emission-absorption measure-

Table 5. Physical parameters of the three samples of H I profiles in Figure 8

	W_{HI} (K km s ⁻¹)	$N_{\text{HI}}^{\text{model}}$ (10 ²⁰ cm ⁻²)	$N_{\text{HI}}^{\text{thin}}$ (10 ²⁰ cm ⁻²)	$N_{\text{HI}}^{\text{model}}/N_{\text{HI}}^{\text{thin}}$	$\langle T_s \rangle$ (K)	$\int \tau_{\text{HI}}^{\text{model}}(V)dV$ (km s ⁻¹)
(1)	(2)	(3)	(4)	(5)	(6)	(7)
Sample P (Figure 8(a)–(c)-P)						
whole	354	7.4	6.5	1.1	200	2.0
WNM	223	4.8	4.1	1.2	2505	0.11
CNM	131	2.6	2.4	1.1	73	1.9
Sample Q (Figure 8(a)–(c)-Q)						
whole	353	10.7	6.4	1.7	82	7.2
WNM	198	3.9	3.6	1.1	3523	0.06
CNM	155	6.8	2.8	2.4	53	7.1
Sample R (Figure 8(a)–(c)-R)						
whole	356	14.5	6.4	2.3	33	25.0
WNM	158	3.4	2.9	1.2	1136	0.17
CNM	198	11.1	3.6	3.1	25	24.8

NOTE— Columns (2): velocity-integrated intensity, (3): column density of the model, (4): column density obtained under the optically-thin assumption (Equation (1)), (5): ratio of (3) to (4), (6): density-weighted harmonic mean of T_s along the lines-of-sight (Eq. 16), (7): velocity-integrated model optical-depth.

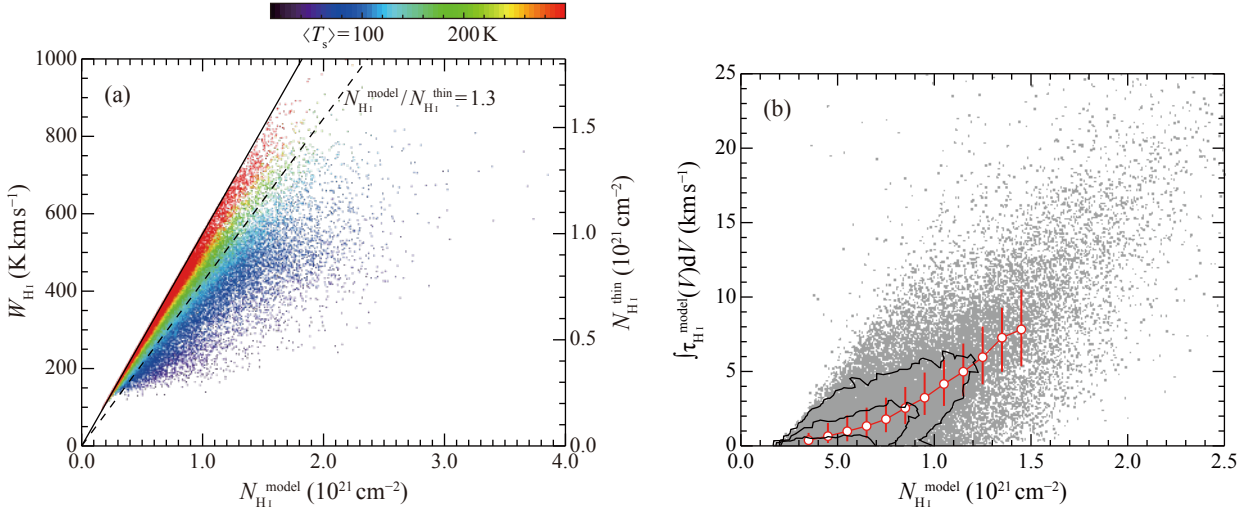


Figure 11. (a) Correlation plot of W_{HI} versus $N_{\text{HI}}^{\text{model}}$. Color represents $\langle T_s \rangle$ of each point. The right-side vertical axis shows the column density given assuming optically thin approximation, $N_{\text{HI}}^{\text{thin}} = 1.823 \times 10^{18} \text{ (cm}^{-2} \text{ K}^{-1} \text{ km}^{-1} \text{ s)}$ W_{HI} . The solid and dashed lines indicate optically thin limit ($N_{\text{HI}}^{\text{model}}/N_{\text{HI}}^{\text{thin}} = 1.0$) and $N_{\text{HI}}^{\text{model}}/N_{\text{HI}}^{\text{thin}} = 1.3$, respectively. (b) Scatter plot between $N_{\text{HI}}^{\text{model}}$ and $\int \tau_{\text{HI}}^{\text{model}}(V)dV$. The circles and vertical bars show the median and interquartile range of $\int \tau_{\text{HI}}^{\text{model}}(V)dV$ in each $1 \times 10^{20} \text{ cm}^{-2}$ bin.

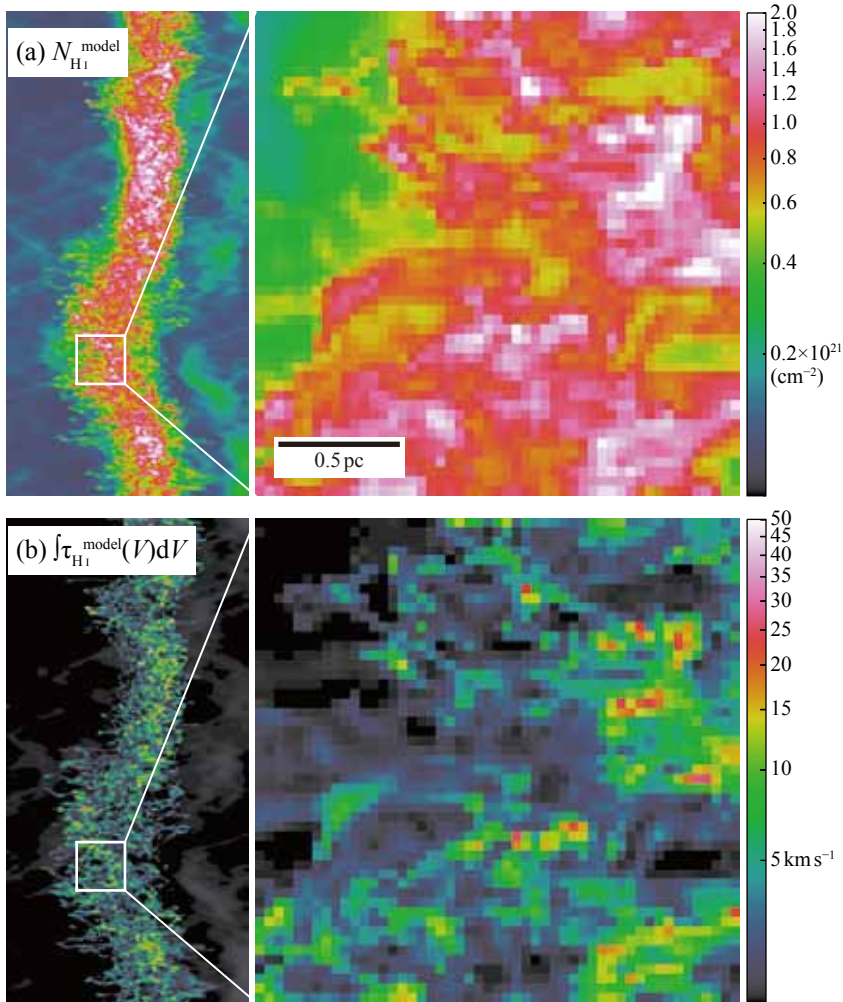


Figure 12. (a) The left panel shows spatial distribution of $N_{\text{HI}}^{\text{model}}$ (identical to Figure 9(d)), and the right panel shows a close-up view of the bounding box overlaid on the left panel. (b) Same as (a) but for $\int \tau_{\text{HI}}^{\text{model}}(V) dV$.

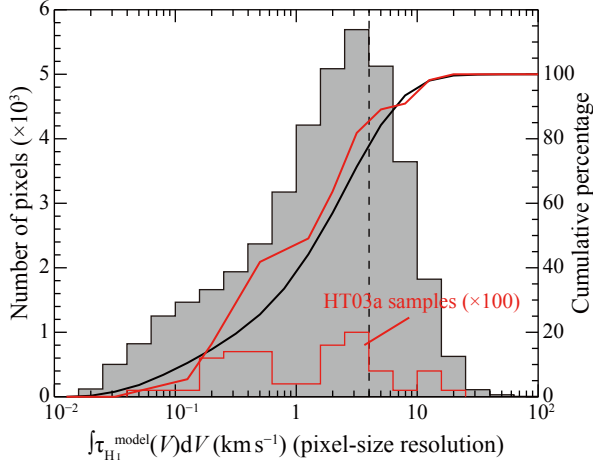


Figure 13. Histogram of $\int \tau_{\text{HI}}^{\text{model}}(V)dV$ at pixel-sized resolution. The dashed line shows $\int \tau_{\text{HI}}^{\text{model}}(V)dV = 4 \text{ km s}^{-1}$ and the black solid curve shows cumulative percentage plotted against right-side vertical-axis. Histogram and cumulative percentage of $\int \tau_{\text{HI}}^{\text{abs}}(V)dV$ of Heiles & Troland (2003a) samples with $|b| > 15^\circ$ (Table 6) are overlaid by the red lines (the former is multiplied by a factor of 100).

ments toward radio continuum compact sources, where $\int \tau_{\text{HI}}^{\text{abs}}(V)dV$ is often used as an observable quantity which characterizes H I gas property in the previous papers (e.g., Stanimirović et al. 2014). The effective resolution in the absorption measurements is given by the size of the radio continuum source and is typically $\lesssim 20''\text{--}30''$ (Heiles & Troland 2003a; Stanimirović et al. 2014), nearly consistent with the present pixel size $0.9''$. The number density of radio sources in the published measurements is small. In the Perseus region (Stanimirović et al. 2014; Lee et al. 2015), the number of radio continuum sources is 27 for 500 square degrees, and the source density in Heiles & Troland (2003a) is similar to that (see Table 6). This indicates source density 0.05 deg^{-2} or 0.005 pc^{-2} at 200 pc in the sky, and corresponds to about 0.25 sources in the present H I distribution having $\sim 50 \text{ pc}^2$. The fraction of the sky measured in the emission-absorption measurements is there-

fore as small as $\sim 4 \times 10^{-6}$ if a source diameter is assumed to be $30''$ or 0.03 pc at 200 pc .

The present synthetic observations show that the emission-absorption measurements toward the present model H I gas will obtain $\int \tau_{\text{HI}}(V)dV$ whose probability distribution is given by Figure 13. The measurements will find smaller $\int \tau_{\text{HI}}(V)dV$ less than 4 km s^{-1} at a probability of 70% and less than 1 km s^{-1} at a probability of 40%. Conversely, it is possible that $\int \tau_{\text{HI}}(V)dV$ higher than 10 km s^{-1} is obtained at a probability of 5% toward peaks of the CNM. So, the general trend observed in the emission-absorption measurements is “smaller $\int \tau_{\text{HI}}(V)dV$ ” of $10^{-1} \text{ km s}^{-1}\text{--}10 \text{ km s}^{-1}$ with a large dispersion over two orders of magnitude at a 20% level in Figure 13. It is a question how well the measured τ_{HI} in the emission-absorption measurements represents the H I gas property given the extremely small source number density. The usual assumption of uniform H I gas in the emission-absorption measurements is far from reality in the present model. It is also to be noted that $T_s(V)$ and $\tau_{\text{HI}}(V)$ differs generally in between equations (13) and (14) contrary to the assumption of the emission-absorption measurements.

In order to clarify the implications of the histogram of $\int \tau_{\text{HI}}(V)dV$, we plotted the emission-absorption measurements by Heiles & Troland (2003a) in Figure 13. The measurements show that the percentage of the observed $\int \tau_{\text{HI}}(V)dV$ less than 4 is more than 80%, and that a small fraction of the data points less than 10% show large integrated H I optical depth more than 10. The trend is consistent with the model prediction. The number of the observed points (see the Heiles & Troland (2003a) data listed in Table 6) is, however, very small, ~ 60 , as compared with the data point of the model, causing larger fluctuations than the model histogram.

Table 3 presents the 3D volume filling factor (Column 9) and the projected covering factor of

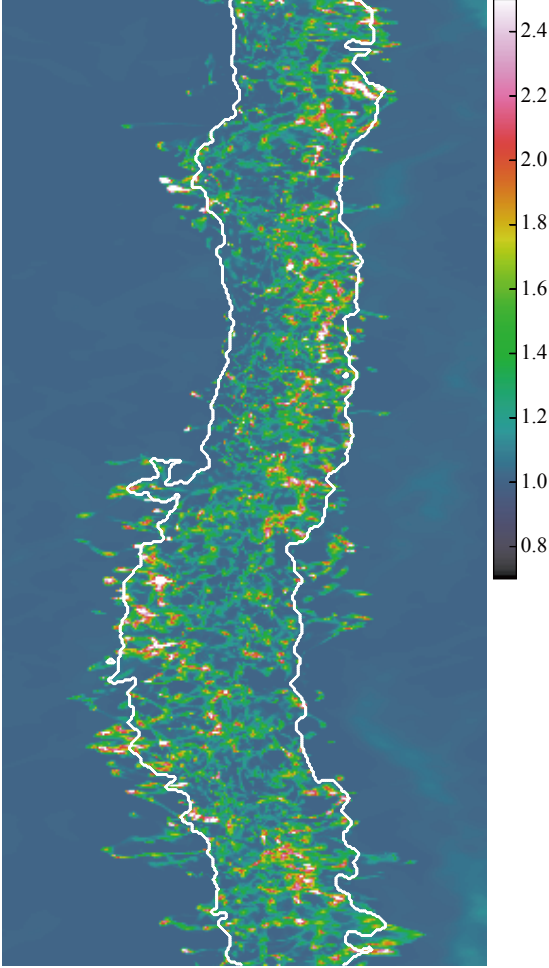


Figure 14. Spatial distribution of the $N_{\text{HI}}^{\text{model}}/N_{\text{HI}}^{\text{thin}}$ ratio at pixel-sized resolution. The contour outlines the ROI (identical to that shown in Figures 1 and 9(g)).

the CNM (Column 10) for all the four epochs. The factors vary gently and show no significant difference among at 0.3 Myrs, 0.5 Myrs, and 1 Myr; for these three epochs the volume filling factor ranges from 3.4% to 5.0% and the covering factor from 29% to 36%. So, the present small covering factor is not limited to the chosen epoch, 0.5 Myr, and we consider the model adopted well approximates the general ISM properties in the solar neighborhood.

4.1.2. Observed value of N_{HI}

N_{HI} does not depend on T_s while τ_{HI} depends on T_s . N_{HI} is therefore a more robust mea-

surable quantity than τ_{HI} . In order to clarify the impact of the inhomogeneous H I distribution on the emission-absorption measurements, we used the $N_{\text{HI}}^{\text{model}}/N_{\text{HI}}^{\text{thin}}$ distribution in Figure 14. It is natural that the distribution is qualitatively similar to the CNM distribution. $N_{\text{HI}}^{\text{model}}/N_{\text{HI}}^{\text{thin}}$ has a tight correspondence with $\int \tau_{\text{HI}}^{\text{model}}(V)dV$; Figure 15(a) shows $N_{\text{HI}}^{\text{model}}/N_{\text{HI}}^{\text{thin}}$ of the present model as a function of $\int \tau_{\text{HI}}^{\text{model}}(V)dV$. Due to significant saturation of W_{HI} in denser regions, $N_{\text{HI}}^{\text{model}}/N_{\text{HI}}^{\text{thin}}$ increases with $\int \tau_{\text{HI}}^{\text{model}}(V)dV$. $\int \tau_{\text{HI}}^{\text{model}}(V)dV = 4 \text{ km s}^{-1}$ corresponds to $N_{\text{HI}}^{\text{model}}/N_{\text{HI}}^{\text{thin}} = 1.3$, which we consider as the boundary beyond which a significant underestimate of $N_{\text{HI}}^{\text{model}}/N_{\text{HI}}^{\text{thin}}$, more than 1.3 to higher than 2, happens in the optically thin approximation.

Figure 15(b) presents a histogram of $N_{\text{HI}}^{\text{model}}/N_{\text{HI}}^{\text{thin}}$. This shows a similar trend with Figure 13 and indicates that more than 70% of the pixels have $N_{\text{HI}}^{\text{model}}/N_{\text{HI}}^{\text{thin}}$ less than 1.3 and that almost 50% of them show $N_{\text{HI}}^{\text{model}}/N_{\text{HI}}^{\text{thin}}$ less than 1.15; we note that in the present model a ratio of the total H I mass of the model relative to the optically thin limit is 1.3 (Table 3). It is thus likely that the emission-absorption measurements underestimate the H I mass for the majority (70%) of the measurements.

Figure 15 shows comparisons with the emission-absorption measurements by Heiles & Troland (2003a), where $N_{\text{HI}}^{\text{model}}$ is replaced by $N_{\text{HI}}^{\text{HT}}$ obtained by the authors (Table 6). Figure 15(a) shows that the behavior of $N_{\text{HI}}^{\text{HT}}/N_{\text{HI}}^{\text{thin}}$ is similar to the model prediction, whereas there is a trend that the observed ratio tends to be smaller than the model. For instance, at velocity integrated H I optical depth of 4, $N_{\text{HI}}/N_{\text{HI}}^{\text{thin}}$ is 1.3 in the model and is 1.1–1.2 in the measurements. This trend becomes more apparent in Figure 15(b), the histogram of $N_{\text{HI}}/N_{\text{HI}}^{\text{thin}}$. The fraction of the $N_{\text{HI}}/N_{\text{HI}}^{\text{thin}}$ points less than 1.3 occupies more than 90% as compared with 70% of the model prediction. It is not clear what

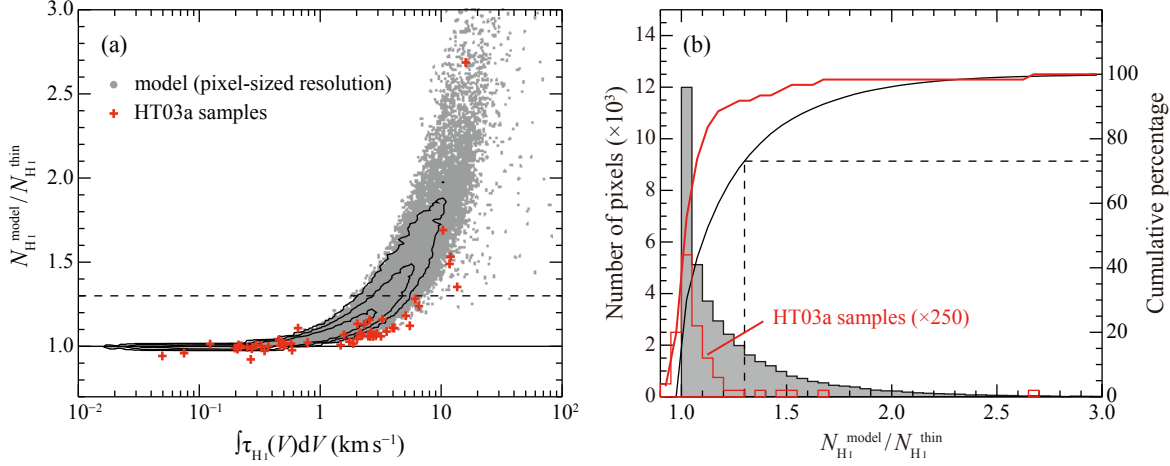


Figure 15. (a) Scatter plot between $\int \tau_{\text{HI}}^{\text{model}}(V)dV$ and $N_{\text{HI}}^{\text{model}}/N_{\text{HI}}^{\text{thin}}$ at pixel-sized resolution. Contours include 50%, 75% and 90% of data points. The solid and dashed lines show $N_{\text{HI}}^{\text{model}}/N_{\text{HI}}^{\text{thin}} = 1.0$ and 1.3, respectively. The red crosses show scatter plot between $\int \tau_{\text{HI}}^{\text{abs}}(V)dV$ and $N_{\text{HI}}^{\text{HT}}/N_{\text{HI}}^{\text{thin}}$ for Heiles & Troland (2003a) samples (table 6). (b) Histogram of $N_{\text{HI}}^{\text{model}}/N_{\text{HI}}^{\text{thin}}$ ratio at pixel-sized resolution. The dashed line shows $N_{\text{HI}}^{\text{model}}/N_{\text{HI}}^{\text{thin}} = 1.3$ and the black solid curve shows cumulative percentage plotted against right-side vertical axis. Histogram and cumulative percentage of $N_{\text{HI}}^{\text{HT}}/N_{\text{HI}}^{\text{thin}}$ ratio of Heiles & Troland (2003a) samples with $|b| > 15^\circ$ (Table 6) are overlaid by the red lines (the former is multiplied by a factor of 250).

is the cause of the difference. A possibility may be that the emission-absorption measurements tend to underestimate N_{HI} . As noted by Heiles & Troland (2003a,b), the fraction of the WNM is still uncertain in the emission-absorption measurements. Absorption by the CNM also reduces N_{HI} as shown by the present model (see Table 5). Correction may be needed to recover the contribution of the WNM in N_{HI} . We note that $\int \tau_{\text{HI}}(V)dV$ (Figure 13) is not affected by the WNM.

In summary, H I gas has highly complicated sub-pc spatial distribution of $\int \tau_{\text{HI}}(V)dV$ according to the current MHD model. The fraction of the solid angle subtended by the radio continuum sources is small, less than 10^{-5} , in the published emission-absorption measurements. The model predicts a large dispersion in $N_{\text{HI}}^{\text{model}}/N_{\text{HI}}^{\text{thin}}$ reflecting the small scale structure of the CNM, which hampers to derive a representative value of N_{HI} and the emission-absorption measurements are not suited for determining the bulk properties of the H I gas.

4.1.3. Possible model dependence

In the present paper we used a model of the H I distribution which was obtained by the state-of-the-art hydrodynamical simulations including the chemical evolution, the magnetic field, and the heating/cooling (Inoue & Inutsuka 2012). There are no other simulations at an equal level in the literature; e.g., in Hennebelle et al. (2008) turbulence is included but no magnetic field is incorporated. The simulations by Valdivia et al. (2016) only include all these processes, whereas their time step is coarser than the present one, and is not suited to the present purpose to fit the UV measurements of H_2 . By considering that the model adopted specific initial conditions, it is worthwhile to reexamine if the model is a reasonable realization of the H I gas in the solar neighborhood and how the initial conditions may affect the present results.

The present simulations assume that the magnetic field is parallel with the H I flow direction (the x -axis). The directivity of the initial magnetic field, however, does not dominate the gas motion in the 0.5-Myr model adopted, and it

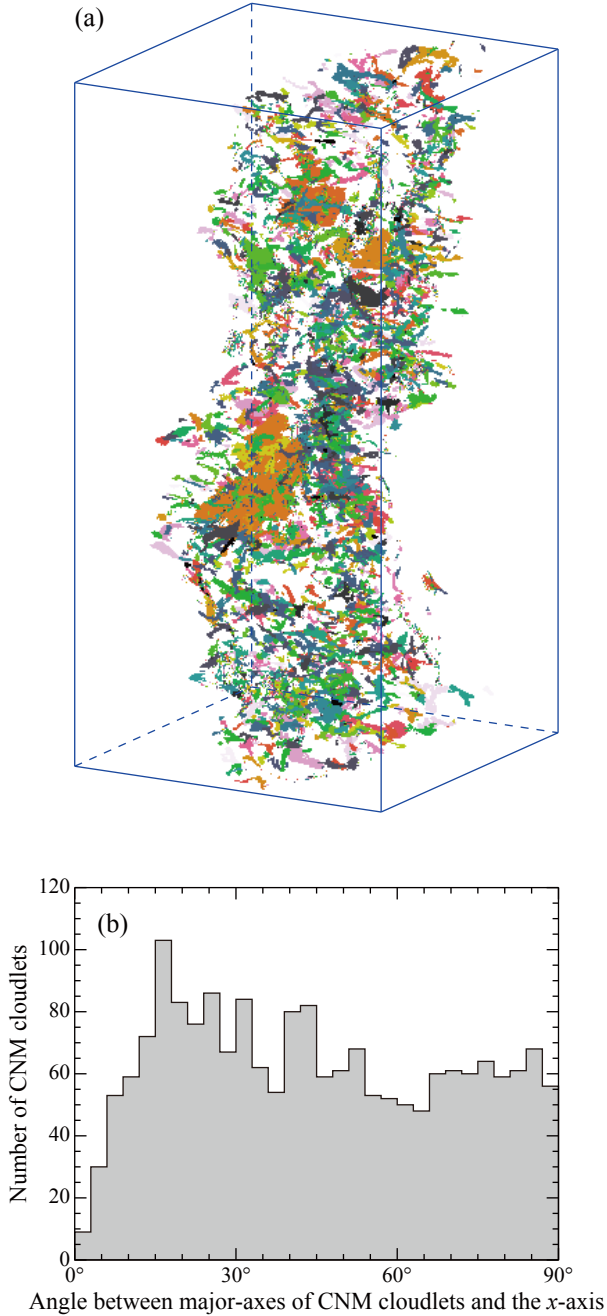


Figure 16. (a) Volume rendering map of the identified CNM cloudlets with $T_s < 300$ K by using the algorithm described in the Appendix of Rosolowsky & Leroy (2006). The colors are randomly allocated to the cloudlets. (b) Histogram of the angle between the elongation of the CNM cloudlets and the x -axis.

is unlikely that the results depend critically on the initial field direction. This is because of the strong randomization by the density inhomogeneities which causes random deformation of the shock fronts. In Figure 12 we see no strong effects of the initial field direction, except for a slight hint of elongation of the CNM along the x -axis. In addition, we analyzed the CNM in Figure 1 and identified 9048 CNM cloudlets as shown in Figure 16(a) by using the decomposition algorithm described in the Appendix of Rosolowsky & Leroy (2006). As a result we identified 1880 cloudlets which show significant elongation (see for details Appendix B), and measured an angle between the elongation of the CNM cloudlets and the x -axis. The histogram of the angle shown in Figure 16(b) lends support for the random orientation of the cloudlets. We also tested several viewing directions in the synthetic observations and confirmed that there is no significant dependence on the directions. So, we conclude the present results of the synthetic observations are not significantly affected by the initial conditions.

The CNM cloudlets are a natural outcome of the turbulent, thermally bistable ISM. The present simulations study the shock propagation of the existing two-phase medium that is not thermally unstable. The shock makes the medium thermally unstable. Physical thermal conduction is involved in the simulations so that most unstable scale of the thermal instability is resolved. Even after the saturation of the thermal instability, the CNM cloudlets do not form broad large-scale structure because the CNM cloudlets fragment again due to corrugation instability (see Inoue et al. 2006; Stone et al. 2008). Survival of sub-pc scale cloudlets is confirmed even after ~ 70 Myr evolution in Figure 7 of Koyama & Inutsuka (2006).

4.2. The Resolution Issue

The original resolution of our simulations is 0.02 pc and the synthetic observations were

made after smoothing by a factor of two into 0.04 pc, which was preferred in the present work in order to save the 3-d data size. The typical width of the CNM filaments is ~ 0.1 pc, which is marginally resolved by the present grid 0.04 pc. This limited resolution is however not a problem in the above discussion on the covering factor, because the covering factor will not vary significantly as reasoned below; the mass spectrum of the CNM is expressed as $dN/dM \propto M^{-1.7}$ according to the simulations as shown by Inoue & Inutsuka (2012) and Hennebelle et al. (2008). If we assume that the CNM follows this relation down to lower M and that the cross section of a CNM cloudlet S is proportional to M for a filamentary shape, the covering factor of CNM is then given by $NS \sim M^{0.3}$ that shows small dependence on mass (or scale) of the CNM. This means spatial resolution better than sub-pc does not change significantly the covering factor and justifies the present pixel size. In this connection, we note on the resolution in Kim et al. (2014) used in the two 21-SPONGE papers (Murray et al. 2015, 2016) was 2 pc for a total length of the simulation box 2 kpc. This grid size was chosen because these simulations were intended to be applied to a kpc scale H I distribution. A 2-pc resolution is however too coarse to resolve the sub-pc filaments of the CNM (see Figure 12) and is not able to probe details of the emission-absorption measurements discussed in the present paper.

4.3. Recent Observations of H I Filaments/Fibers

The spatial distribution of the CNM has been a subject of H I observations since 1970s. Based on aperture synthesis of the H I absorption toward extended continuum sources, Greisen (1973a,b) claimed that the CNM was clumpy. Subsequent observations in absorption toward extended sources and double continuum sources provided some observational constraints on the CNM distribution (Payne et al. 1982; Dickey

1979), whereas these studies were not able to constrain the covering factor of the CNM. Heiles (1997) made observations toward sharp gradients in optical depth on scales of milli-arcseconds and the results support the present conclusion about the compact structure of the CNM.

It is interesting to note that a few recent papers indicate the existence of CNM filaments similar to those presented in the present work. McClure-Griffiths et al. (2006) pointed out such filaments, and Clark et al. (2014) identified the H I filaments by the Rolling Hough Transformation at 16' resolution. They named the CNM filaments ‘‘fibers’’ which has column density of $5 \times 10^{18} \text{ cm}^{-2}$, where $N_{\text{H I}}$ of the extended WNM is 10^{20} cm^{-2} . By unsharp masking Kalberla et al. (2016) identified CNM filaments whose $N_{\text{H I}}$ is $10^{19.1} \text{ cm}^{-2}$ in the local ISM. These CNM filaments/fibers are well aligned with the magnetic field. Inoue & Inutsuka (2016) supported the formation of the CNM filaments and their alignment with the magnetic field based on the MHD simulations. The filaments/fibers appear to have a small covering factor similar to the present CNM filaments (see Figures 3 and 4 of Clark et al. 2014). More quantitatively speaking, we note that the above $N_{\text{H I}}$ of fibers/filaments is crude at best, because the methods based on $W_{\text{H I}}$ alone is not sensitive enough to all $N_{\text{H I}}$ of the CNM; it is difficult to observationally extract $W_{\text{H I}}^{\text{CNM}}$ from $W_{\text{H I}}$ in Figures 9(a) and 9(b). The column density of the H I filament/fibers derived by these authors is in the order of $\sim 10^{19} \text{ cm}^{-2}$, which is about an order of magnitude smaller than that of the present CNM clumps $\sim 10^{20} \text{ cm}^{-2}$. Figure 10(b) shows that 60% of the pixels of the CNM have $N_{\text{H I}} \lesssim 3 \times 10^{20} \text{ cm}^{-2}$. Considering that the mass of the CNM is comparable to that of the WNM, it is unlikely that the filaments/fibers of that column density is dominant as the CNM. In order to test the methods, we applied the unsharp

masking to the present W_{HI} distribution in Figure 9(a) and identified filaments. The result shows that the column density of the filaments is about 20% of that derived as $N_{\text{HI}}^{\text{CNM}}$ in the present CNM filaments. It is possible that the extraction of filaments from W_{HI} is able to detect only part of the CNM and the H I column density in Kalberla et al. (2016) gives a lower value than $N_{\text{HI}}^{\text{CNM}}$. The low resolution 16' employed may also be diluting $N_{\text{HI}}^{\text{CNM}}$ at a sub-pc scale. Future high resolution H I studies will help to better quantify $N_{\text{HI}}^{\text{CNM}}$.

4.4. Importance of Measuring Accurate N_{HI} ; a Potential of the *Planck/IRAS* Based Method

A precise measurement of the bulk H I mass is an important astrophysical issue. As an example, an application of the H I measurements is made toward the gamma-ray SNRs where the hadronic process may play a major role in gamma-ray production (e.g., Aharonian et al. 2006). If the hadronic process, basically a proton-proton collision, is working to create gamma-rays in the SNRs, the gamma-ray distribution should resemble the ISM proton distribution for given fairly uniform distribution of cosmic-ray protons in the SNRs. It is a crucial test to identify the spatial correspondence between the gamma rays and the ISM as already shown in two gamma-ray SNRs, RXJ1713.7–3946 and HESSJ1731–347 by Fukui et al. (2012) and Fukuda et al. (2014).

The emission-absorption measurements biased toward a very small volume is not suited to probe the bulk H I having complicated small-scale fluctuations which acts as the target protons in the hadronic interaction. Conversely, the *Planck/IRAS*-based method with a larger beam of 5' has a potential as a superior tool for measuring the ISM proton mass and distribution (Fukui et al. 2014, 2015) as demonstrated by a recent work on a gamma ray SNR RXJ0852.0–4622 where the *Planck/IRAS*-

based method is successfully employed to calculate proton density with a high precision in the order of $\sim 10\%$ (Fukui et al. 2017). The *Planck/IRAS*-based method utilizes the data in emission and has an advantage to fully map the H I gas, which enables to estimate the total H I mass. This method is to be better confirmed by proving that the dust optical depth gives a reliable proxy of H I via comparison with independent ISM measure like A_V and gamma-ray counts (e.g., Roy et al. 2013; Mizuno et al. 2016). As one of such efforts, in the Perseus cloud, $\int \tau_{\text{HI}}(V)dV$ is estimated for seven radio sources by the emission-absorption measurements (Stanimirović et al. 2014) and by the *Planck/IRAS*-based method (Okamoto et al. 2017). The former gives smaller $\int \tau_{\text{HI}}(V)dV$ from 2 km s^{-1} to 5 km s^{-1} , while the latter from 5 km s^{-1} to 16 km s^{-1} , with an average ratio of about 2 (Okamoto et al. 2017). This difference is not inconsistent with the highly filamentary CNM distribution while the number of sources is limited at present. Future extension of such a comparison to the other regions by achieving higher sensitivity toward radio compact sources will be important.

Further, it is required to better quantify the interstellar molecular hydrogen. X_{CO} for converting the CO emission into hydrogen mass is an important factor to estimate the molecular hydrogen and it is generally thought that X_{CO} may be uncertain by a factor of 2 in the conventional method (e.g., Bolatto et al. 2013). The new method to derive X_{CO} used by Fukui et al. (2014) and Okamoto et al. (2017) is based on the *Planck/IRAS*-data and presented successfully a precise X_{CO} distribution in the MBM 53–55 and Perseus clouds. This method of estimating X_{CO} is a promising one to provide N_{H_2} with a high accuracy of $\lesssim 10\%$, comparable to the present estimate of N_{HI} , indicating a potential of the *Planck/IRAS*-based method.

5. CONCLUSIONS

In order to gain an insight into the detailed physical conditions of the interstellar H I gas and their observed properties in the solar neighborhood, we carried out synthetic observations of the interstellar H I gas at 21 cm by using the MHD numerical simulations of the realistic inhomogeneous H I gas which is in the converging flows (Inoue & Inutsuka 2012). The simulations incorporate the microscopic processes including the H₂ formation reactions, the magnetic field, and the heating/cooling. The simulated H I gas is highly turbulent and inhomogeneous and is far from equilibrium with a typical dynamical timescale in the order of Myr. The results were compared with the conventional emission-absorption measurements. The main conclusions of the present study are summarized as follows;

1. The present analysis was made for the model at an evolutionary epoch of 0.5 Myrs, which was chosen from the simulation results covering a time span of 10 Myrs. The model reproduces the distribution of the H₂ fraction f_{H_2} which is consistent with the ultraviolet measurements of H₂. As shown by the previous works over the last five decades, the H I gas consists of the two components, the CNM (cold neutral medium) and the WNM (warm neutral medium). The CNM has spin temperature T_s ranging from 10 K to 300 K and the WNM from 300 K to 10000 K. The density range of the CNM is from 10 cm^{-3} to 10^3 cm^{-3} and that of the WNM from 1 cm^{-3} to 100 cm^{-3} . The synthetic observations show that the CNM has a small volume filling factor of 3.5%, whereas the WNM is distributed with a volume filling factor of 96.5%, while the gas mass of each component is comparable. These filling factors are consistent with the peak density of the CNM larger than that of the WNM by a factor of ~ 30 .

The CNM distribution is highly clumpy and filamentary with a sub-pc size scale and the WNM distribution is smooth with much less small-scale structures. As a result, the CNM covering factor is small, $\sim 30\%$, in the sky. These represent general properties of the H I gas in the solar neighborhood.

2. H I line profiles were calculated by separating the CNM and WNM. The CNM is seen as a narrow feature of $\sim 5 \text{ km s}^{-1}$ in half-power full linewidth and the WNM as a wing-like feature spanning over $\sim 40 \text{ km s}^{-1}$. These properties are consistent with the observed H I profiles, lending support for the chosen model. By setting background radiation, absorption line profiles toward radio continuum sources were also synthesized. The H I distributions in the sky were reproduced in the 21 cm line integrated intensity ($W_{\text{H I}}$), the H I column density ($N_{\text{H I}}$), and the velocity integrated optical depth ($\tau_{\text{H I}}$), both for the CNM and WNM separately. Saturation of $W_{\text{H I}}$ due to high $\int \tau_{\text{H I}}(V)dV$ greater than 2 km s^{-1} is significant in about half of the H I gas. This lends support for the optically thick H I presented by Fukui et al. (2015). $\tau_{\text{H I}}$ is dominated by the CNM. The contribution of the WNM in $\tau_{\text{H I}}$ is negligibly small due to the T_s^{-1} -dependence of the H I opacity.
3. The properties of the CNM distribution were compared with the observations in a histogram of $\int \tau_{\text{H I}}(V)dV$. It is notable that the fraction of $\tau_{\text{H I}}$ less than 4 km s^{-1} corresponds to 80% of the observed pixels, indicating that the conventional emission-absorption measurements preferentially sample smaller $\tau_{\text{H I}}$ of the WNM. This reflects the large covering factor of the WNM. In addition, the nonlinear dependence of $\tau_{\text{H I}}$ as (density)² causes

spatial variation of τ_{HI} larger than that of N_{HI} . The model explains the usual small H I optical depth obtained by the conventional emission-absorption measurements (Heiles & Troland 2003a,b). Conversely, the fraction of $\int \tau(V)dV$ greater than 2 km s^{-1} is $\sim 50\%$, and the real H I optical depth is large enough to cause significant saturation in W_{HI} for about half of the total H I mass.

4. The present model indicates that N_{HI} is close to the optically thin limit within a factor of 1.3 at $\sim 70\%$ of the observed pixels and within a factor of 1.15 at $\sim 50\%$ of the pixels. Conversely, pixels with the actual N_{HI} larger than the optically thin case by a factor of 1.3 occupies $\sim 30\%$ of the pixels. It is usually considered that N_{HI} is consistent with the optically thin limit, whereas the real H I mass of the model is 1.3 times larger than the optically thin approximation. The optically thin approximation thus leads to underestimate the H I mass by a factor of 1.3, which causes non-negligible errors in estimating interstellar protons.
5. A detailed comparison of the model with N_{HI} derived from the conventional emission-absorption measurements indicates that the observed N_{HI} tends to be systematically smaller than N_{HI} in the model by a factor of ~ 1.2 . It is not entirely clear how N_{HI} was underestimated in the conventional method. A possibility may be the uncertainty in the contribution of the WNM whose real intensity is not as accurate as in τ_{HI} .

In summary, we studied the detailed properties of the interstellar H I gas in the solar neighborhood, and made it clear that the CNM has significant sub-pc structures with a small covering factor in the sky. We showed the observed quantities in the conventional emission-absorption measurements toward radio continuum point sources are subject to an observational bias toward the WNM having a large covering factor. This bias leads to underestimate τ_{HI} and N_{HI} . Accordingly, the conventional H I mass is required to be revised upward by a factor of 1.3 in the present model. The present results provide a step forward toward more accurate determination of the interstellar proton mass. The mass is crucial for identifying the ISM target protons, for instance, in cosmic-ray proton reactions in the gamma-ray SNRs. The results are qualitatively consistent with the *Planck/IRAS*-based analysis of H I by Fukui et al. (2014, 2015), while a more quantitative pursuit remains as future work, including a test of the nonlinear behavior of the sub-mm dust optical depth due to dust evolution and an extension to the whole sky.

We are grateful to John Dickey for his thoughtful comments which were valuable in improving significantly the present paper. The useful comments by the referee helped to improve the content and readability of the paper. This work was supported by JSPS KAKENHI Grant Number JP15H05694. Based on observations obtained with *Planck* (<http://www.esa.int/Planck>), an ESA science mission with instruments and contributions directly funded by ESA Member States, NASA, and Canada. Some of the results in this paper have been derived using the HEALPix (Górski et al. 2005) package. This research has made use of the VizieR catalogue access tool, CDS, Strasbourg, France.

APPENDIX

A. RESULTS OF THE EMISSION-ABSORPTION MEASUREMENTS BY HEILES & TROLAND (2003A)

Table 6 gives the results of the emission-absorption measurements by Heiles & Troland (2003a). Sixty-one sources which lie at $|b|$ greater than 15° are selected. Each column is explained in the footnotes.

Table 6. Physical parameters of H I toward radio continuum sources

Name	l	b	W_{HI} (K km s $^{-1}$)	$\int \tau_{\text{HI}}^{\text{abs}}(V)dV$ (km s $^{-1}$)	$N_{\text{HI}}^{\text{HT}}$ (10^{20} cm $^{-2}$)	$N_{\text{HI}}^{\text{thin}}$ (10^{20} cm $^{-2}$)	$N_{\text{HI}}^{\text{HT}}/N_{\text{HI}}^{\text{thin}}$
(1)	(2)	(3)	(4)	(5)	(6)	(7)	(8)
3C18	118 $^\circ$ 62	−52 $^\circ$ 72	283	3.26	5.99	5.17	1.16
3C33-1	129 $^\circ$ 43	−49 $^\circ$ 34	154	0.37	2.81	2.81	1.00
3C33	129 $^\circ$ 44	−49 $^\circ$ 32	154	0.27	2.78	2.82	0.98
3C33-2	129 $^\circ$ 46	−49 $^\circ$ 27	164	0.59	2.92	2.99	0.97
3C64	157 $^\circ$ 76	−48 $^\circ$ 20	333	2.02	6.33	6.08	1.04
3C75-1	170 $^\circ$ 21	−44 $^\circ$ 91	412	2.49	7.97	7.53	1.06
3C75	170 $^\circ$ 25	−44 $^\circ$ 91	409	2.73	7.89	7.46	1.06
3C75-2	170 $^\circ$ 29	−44 $^\circ$ 91	427	2.59	8.23	7.78	1.06
3C78	174 $^\circ$ 85	−44 $^\circ$ 51	497	3.97	10.06	9.08	1.11
3C79	164 $^\circ$ 14	−34 $^\circ$ 45	473	3.54	9.37	8.63	1.09
CTA21	166 $^\circ$ 63	−33 $^\circ$ 59	483	2.63	9.56	8.82	1.08
P0320+05	176 $^\circ$ 98	−40 $^\circ$ 84	548	5.51	11.20	10.00	1.12
NRAO140	159 $^\circ$ 00	−18 $^\circ$ 76	603	15.96	29.49	11.00	2.68
3C93.1	160 $^\circ$ 03	−15 $^\circ$ 91	528	6.10	12.32	9.63	1.28
P0347+05	182 $^\circ$ 27	−35 $^\circ$ 73	625	5.10	13.45	11.40	1.18
3C98-1	179 $^\circ$ 85	−31 $^\circ$ 08	537	3.18	10.37	9.80	1.06
3C98	179 $^\circ$ 83	−31 $^\circ$ 04	546	4.08	11.02	9.97	1.11
3C98-2	179 $^\circ$ 82	−31 $^\circ$ 02	523	2.93	10.25	9.55	1.07
3C105	187 $^\circ$ 63	−33 $^\circ$ 60	526	11.97	14.68	9.60	1.53
3C109	181 $^\circ$ 82	−27 $^\circ$ 77	767	11.73	20.82	14.00	1.49
P0428+20	176 $^\circ$ 80	−18 $^\circ$ 55	970	13.57	23.89	17.69	1.35
3C120	190 $^\circ$ 37	−27 $^\circ$ 39	517	10.35	15.94	9.44	1.69
DW0742+1	209 $^\circ$ 79	16 $^\circ$ 59	134	−0.26	2.43	2.45	0.99

Table 6 continued

Table 6 (*continued*)

Name	l	b	W_{HI} (K km s ⁻¹)	$\int \tau_{\text{HI}}^{\text{abs}}(V)dV$ (km s ⁻¹)	$N_{\text{HI}}^{\text{HT}}$ (10 ²⁰ cm ⁻²)	$N_{\text{HI}}^{\text{thin}}$ (10 ²⁰ cm ⁻²)	$N_{\text{HI}}^{\text{HT}}/N_{\text{HI}}^{\text{thin}}$
(1)	(2)	(3)	(4)	(5)	(6)	(7)	(8)
3C190.0	207°62	21°84	160	-0.06	2.82	2.93	0.96
3C192	197°91	26°40	216	0.50	3.97	3.95	1.01
P0820+22	201°36	29°67	231	0.47	4.23	4.22	1.00
3C207	212°96	30°13	271	2.21	5.25	4.95	1.06
3C208.0	213°66	33°16	165	0.27	2.99	3.02	0.99
3C208.1	213°60	33°58	151	0.33	2.76	2.76	1.00
3C223	188°40	48°65	57	0.27	0.96	1.04	0.92
3C225a	219°86	44°02	183	0.57	3.40	3.35	1.01
3C225b	220°01	44°00	179	1.48	3.28	3.26	1.01
3C228.0	220°83	46°63	147	0.35	2.61	2.69	0.97
3C234	200°20	52°70	87	0.12	1.61	1.59	1.01
3C236	190°06	53°98	64	-0.14	1.21	1.18	1.03
3C237	232°11	46°62	109	0.66	2.20	1.99	1.11
3C245	233°12	56°30	116	0.07	2.03	2.12	0.96
P1055+20	222°51	63°13	85	0.29	1.57	1.56	1.01
P1117+14	240°43	65°78	86	0.22	1.57	1.57	1.00
3C263.1	228°27	74°37	91	0.21	1.68	1.67	1.01
3C264.0	236°99	73°64	95	0.25	1.73	1.75	0.99
3C267.0	256°34	70°11	127	0.22	2.33	2.33	1.00
3C272.1	280°63	74°68	132	0.20	2.39	2.42	0.99
3C273	289°94	64°35	107	0.21	1.93	1.97	0.98
3C274.1	269°87	83°16	124	0.46	2.36	2.27	1.04
4C07.32	322°22	68°83	113	0.49	2.11	2.08	1.02
4C32.44	67°23	81°04	61	0.05	1.05	1.12	0.94
3C286	56°52	80°67	110	-1.26	2.04	2.02	1.01
3C293	54°60	76°06	70	-0.01	1.28	1.28	1.00
4C19.44	8°99	73°04	144	-0.39	2.65	2.63	1.01
4C20.33	20°18	66°83	146	0.51	2.69	2.67	1.01
3C310	38°50	60°20	190	1.57	3.71	3.48	1.07
3C315	39°36	58°30	226	2.56	4.77	4.13	1.15
3C318	29°98	54°78	230	2.03	4.75	4.20	1.13
3C333	37°30	42°97	247	2.31	5.09	4.51	1.13

Table 6 continued

Table 6 (*continued*)

Name	l	b	W_{HI} (K km s ⁻¹)	$\int \tau_{\text{HI}}^{\text{abs}}(V)dV$ (km s ⁻¹)	$N_{\text{HI}}^{\text{HT}}$ (10 ²⁰ cm ⁻²)	$N_{\text{HI}}^{\text{thin}}$ (10 ²⁰ cm ⁻²)	$N_{\text{HI}}^{\text{HT}}/N_{\text{HI}}^{\text{thin}}$
(1)	(2)	(3)	(4)	(5)	(6)	(7)	(8)
3C348	22°:97	29°:17	289	2.15	5.69	5.28	1.08
3C353	21°:11	19°:87	481	6.55	10.85	8.77	1.24
4C13.65	39°:31	17°:71	473	2.88	9.16	8.64	1.06
3C433	74°:47	-17°:69	426	1.88	7.89	7.77	1.01
3C454.0	88°:10	-35°:94	289	0.79	5.38	5.27	1.02
3C454.3	86°:11	-38°:18	349	1.74	6.53	6.37	1.03

NOTE— Columns (1): name of target, (2) and (3): position in the Galactic coordinates, (4)–(6): H I parameters given from Heiles & Troland (2003a) dataset; velocity-integrated intensity derived from expected profile, velocity-integrated optical-depth derived from opacity profile, and column density, (7): column density obtained under assumption of optically-thin H I line, (8): ratio of (6) and (7).

B. THE ELONGATION AXES OF THE CNM CLOUDLETS

The orientation of the elongated CNM cloudlets are determined by using a principal component analysis (PCA). This method were adopted to determine the position angle of molecular clouds (e.g., Koda et al. 2006; Rosolowsky & Leroy 2006).

The density-weighted covariance matrix for a cloudlet is given as

$$C = \frac{1}{\sum_i n_i} \begin{pmatrix} C_{x,x} & C_{x,y} & C_{x,z} \\ C_{x,y} & C_{y,y} & C_{y,z} \\ C_{x,z} & C_{y,z} & C_{z,z} \end{pmatrix}, \quad (\text{B1})$$

where

$$C_{x,x} = \sum_i n_i (x_i - \bar{x})^2$$

$$C_{x,y} = \sum_i n_i (x_i - \bar{x})(y_i - \bar{y})$$

$$C_{x,z} = \sum_i n_i (x_i - \bar{x})(z_i - \bar{z})$$

$$C_{y,y} = \sum_i n_i (y_i - \bar{y})^2$$

$$C_{y,z} = \sum_i n_i (y_i - \bar{y})(z_i - \bar{z})$$

$$C_{z,z} = \sum_i n_i (z_i - \bar{z})^2,$$

x_i , y_i and z_i are coordinates in the numerical domain, n_i is H I density of the i -th pixel in the cloudlet, and \bar{x} , \bar{y} and \bar{z} are the density-weighted mean position of the cloudlet. We define the elongation axis to lie along the eigenvector with the largest eigenvalue if $|\det C| > 10^{-6}$.

REFERENCES

- Aharonian, F., Akhperjanian, A. G., Bazer-Bachi, A. R., et al. 2006, *A&A*, 449, 223, doi: 10.1051/0004-6361:20054279
- Banerjee, R., Vázquez-Semadeni, E., Hennebelle, P., & Klessen, R. S. 2009, *MNRAS*, 398, 1082, doi: 10.1111/j.1365-2966.2009.15115.x

- Blitz, L., & Rosolowsky, E. 2006, *ApJ*, 650, 933, doi: [10.1086/505417](https://doi.org/10.1086/505417)
- Bolatto, A. D., Wolfire, M., & Leroy, A. K. 2013, *ARA&A*, 51, 207, doi: [10.1146/annurev-astro-082812-140944](https://doi.org/10.1146/annurev-astro-082812-140944)
- Braun, R. 2012, *ApJ*, 749, 87, doi: [10.1088/0004-637X/749/1/87](https://doi.org/10.1088/0004-637X/749/1/87)
- Clark, S. E., Peek, J. E. G., & Putman, M. E. 2014, *ApJ*, 789, 82, doi: [10.1088/0004-637X/789/1/82](https://doi.org/10.1088/0004-637X/789/1/82)
- Dickey, J. M. 1979, *ApJ*, 233, 558, doi: [10.1086/157416](https://doi.org/10.1086/157416)
- Dickey, J. M., McClure-Griffiths, N. M., Gaensler, B. M., & Green, A. J. 2003, *ApJ*, 585, 801, doi: [10.1086/346081](https://doi.org/10.1086/346081)
- Draine, B. T. 2011, *Physics of the Interstellar and Intergalactic Medium* (Princeton University Press)
- Ewen, H. I., & Purcell, E. M. 1951, *Nature*, 168, 356, doi: [10.1038/168356a0](https://doi.org/10.1038/168356a0)
- Field, G. B. 1965, *ApJ*, 142, 531, doi: [10.1086/148317](https://doi.org/10.1086/148317)
- Field, G. B., Goldsmith, D. W., & Habing, H. J. 1969, *ApJL*, 155, L149, doi: [10.1086/180324](https://doi.org/10.1086/180324)
- Field, G. B., & Saslaw, W. C. 1965, *ApJ*, 142, 568, doi: [10.1086/148318](https://doi.org/10.1086/148318)
- Fukuda, T., Yoshiike, S., Sano, H., et al. 2014, *ApJ*, 788, 94, doi: [10.1088/0004-637X/788/1/94](https://doi.org/10.1088/0004-637X/788/1/94)
- Fukui, Y., & Kawamura, A. 2010, *ARA&A*, 48, 547, doi: [10.1146/annurev-astro-081309-130854](https://doi.org/10.1146/annurev-astro-081309-130854)
- Fukui, Y., Torii, K., Onishi, T., et al. 2015, *ApJ*, 798, 6, doi: [10.1088/0004-637X/798/1/6](https://doi.org/10.1088/0004-637X/798/1/6)
- Fukui, Y., Mizuno, N., Yamaguchi, R., et al. 1999, *PASJ*, 51, 745, doi: [10.1093/pasj/51.6.745](https://doi.org/10.1093/pasj/51.6.745)
- Fukui, Y., Kawamura, A., Minamidani, T., et al. 2008, *ApJS*, 178, 56, doi: [10.1086/589833](https://doi.org/10.1086/589833)
- Fukui, Y., Kawamura, A., Wong, T., et al. 2009, *ApJ*, 705, 144, doi: [10.1088/0004-637X/705/1/144](https://doi.org/10.1088/0004-637X/705/1/144)
- Fukui, Y., Sano, H., Sato, J., et al. 2012, *ApJ*, 746, 82, doi: [10.1088/0004-637X/746/1/82](https://doi.org/10.1088/0004-637X/746/1/82)
- Fukui, Y., Okamoto, R., Kaji, R., et al. 2014, *ApJ*, 796, 59, doi: [10.1088/0004-637X/796/1/59](https://doi.org/10.1088/0004-637X/796/1/59)
- Fukui, Y., Sano, H., Sato, J., et al. 2017, *ArXiv e-prints*. <https://arxiv.org/abs/1708.07911>
- Gillmon, K., Shull, J. M., Tumlinson, J., & Danforth, C. 2006, *ApJ*, 636, 891, doi: [10.1086/498053](https://doi.org/10.1086/498053)
- Górski, K. M., Hivon, E., Banday, A. J., et al. 2005, *ApJ*, 622, 759, doi: [10.1086/427976](https://doi.org/10.1086/427976)
- Greisen, E. W. 1973a, *ApJ*, 184, 363, doi: [10.1086/152336](https://doi.org/10.1086/152336)
- . 1973b, *ApJ*, 184, 379, doi: [10.1086/152337](https://doi.org/10.1086/152337)
- Grenier, I. A., Black, J. H., & Strong, A. W. 2015, *ARA&A*, 53, 199, doi: [10.1146/annurev-astro-082214-122457](https://doi.org/10.1146/annurev-astro-082214-122457)
- Grenier, I. A., Casandjian, J.-M., & Terrier, R. 2005, *Science*, 307, 1292, doi: [10.1126/science.1106924](https://doi.org/10.1126/science.1106924)
- Heiles, C. 1997, *ApJ*, 481, 193, doi: [10.1086/304033](https://doi.org/10.1086/304033)
- Heiles, C., Kulkarni, S., & Stark, A. A. 1981, *ApJL*, 247, L73, doi: [10.1086/183592](https://doi.org/10.1086/183592)
- Heiles, C., & Troland, T. H. 2003a, *ApJS*, 145, 329, doi: [10.1086/367785](https://doi.org/10.1086/367785)
- . 2003b, *ApJ*, 586, 1067, doi: [10.1086/367828](https://doi.org/10.1086/367828)
- Heitsch, F., Stone, J. M., & Hartmann, L. W. 2009, *ApJ*, 695, 248, doi: [10.1088/0004-637X/695/1/248](https://doi.org/10.1088/0004-637X/695/1/248)
- Hennelbelle, P., Banerjee, R., Vázquez-Semadeni, E., Klessen, R. S., & Audit, E. 2008, *A&A*, 486, L43, doi: [10.1051/0004-6361:200810165](https://doi.org/10.1051/0004-6361:200810165)
- Inoue, T., & Inutsuka, S.-i. 2012, *ApJ*, 759, 35, doi: [10.1088/0004-637X/759/1/35](https://doi.org/10.1088/0004-637X/759/1/35)
- . 2016, *ApJ*, 833, 10, doi: [10.3847/0004-637X/833/1/10](https://doi.org/10.3847/0004-637X/833/1/10)
- Inoue, T., Inutsuka, S.-i., & Koyama, H. 2006, *ApJ*, 652, 1331, doi: [10.1086/508334](https://doi.org/10.1086/508334)
- Kalberla, P. M. W., Burton, W. B., Hartmann, D., et al. 2005, *A&A*, 440, 775, doi: [10.1051/0004-6361:20041864](https://doi.org/10.1051/0004-6361:20041864)
- Kalberla, P. M. W., Kerp, J., Haud, U., et al. 2016, *ApJ*, 821, 117, doi: [10.3847/0004-637X/821/2/117](https://doi.org/10.3847/0004-637X/821/2/117)
- Kawamura, A., Mizuno, Y., Minamidani, T., et al. 2009, *ApJS*, 184, 1, doi: [10.1088/0067-0049/184/1/1](https://doi.org/10.1088/0067-0049/184/1/1)
- Kim, C.-G., Ostriker, E. C., & Kim, W.-T. 2014, *ApJ*, 786, 64, doi: [10.1088/0004-637X/786/1/64](https://doi.org/10.1088/0004-637X/786/1/64)
- Koda, J., Sawada, T., Hasegawa, T., & Scoville, N. Z. 2006, *ApJ*, 638, 191, doi: [10.1086/498640](https://doi.org/10.1086/498640)
- Koyama, H., & Inutsuka, S.-i. 2006, *ArXiv Astrophysics e-prints*
- Lee, M.-Y., Stanimirović, S., Murray, C. E., Heiles, C., & Miller, J. 2015, *ApJ*, 809, 56, doi: [10.1088/0004-637X/809/1/56](https://doi.org/10.1088/0004-637X/809/1/56)
- McClure-Griffiths, N. M., Dickey, J. M., Gaensler, B. M., Green, A. J., & Haverkorn, M. 2006, *ApJ*, 652, 1339, doi: [10.1086/508706](https://doi.org/10.1086/508706)

- McKee, C. F., Parravano, A., & Hollenbach, D. J. 2015, *ApJ*, 814, 13, doi: [10.1088/0004-637X/814/1/13](https://doi.org/10.1088/0004-637X/814/1/13)
- Mizuno, T., Abdollahi, S., Fukui, Y., et al. 2016, *ApJ*, 833, 278, doi: [10.3847/1538-4357/833/2/278](https://doi.org/10.3847/1538-4357/833/2/278)
- Muller, C. A., & Oort, J. H. 1951, *Nature*, 168, 357, doi: [10.1038/168357a0](https://doi.org/10.1038/168357a0)
- Murray, C. E., Stanimirovic, S., Kim, C.-G., et al. 2016, *ArXiv e-prints*, <https://arxiv.org/abs/1612.02017>
- Murray, C. E., Stanimirović, S., Goss, W. M., et al. 2015, *ApJ*, 804, 89, doi: [10.1088/0004-637X/804/2/89](https://doi.org/10.1088/0004-637X/804/2/89)
- Okamoto, R., Yamamoto, H., Tachihara, K., et al. 2017, *ApJ*, 838, 132, doi: [10.3847/1538-4357/aa6747](https://doi.org/10.3847/1538-4357/aa6747)
- Payne, H. E., Terzian, Y., & Salpeter, E. E. 1982, *ApJS*, 48, 199, doi: [10.1086/190775](https://doi.org/10.1086/190775)
- Peek, J. E. G., Heiles, C., Douglas, K. A., et al. 2011, *ApJS*, 194, 20, doi: [10.1088/0067-0049/194/2/20](https://doi.org/10.1088/0067-0049/194/2/20)
- Planck Collaboration. 2014, *A&A*, 571, A11, doi: [10.1051/0004-6361/201323195](https://doi.org/10.1051/0004-6361/201323195)
- Rachford, B. L., Snow, T. P., Tumlinson, J., et al. 2002, *ApJ*, 577, 221, doi: [10.1086/342146](https://doi.org/10.1086/342146)
- Rosolowsky, E., & Leroy, A. 2006, *PASP*, 118, 590, doi: [10.1086/502982](https://doi.org/10.1086/502982)
- Roy, A., Martin, P. G., Polychroni, D., et al. 2013, *ApJ*, 763, 55, doi: [10.1088/0004-637X/763/1/55](https://doi.org/10.1088/0004-637X/763/1/55)
- Stanimirović, S., Murray, C. E., Lee, M.-Y., Heiles, C., & Miller, J. 2014, *ApJ*, 793, 132, doi: [10.1088/0004-637X/793/2/132](https://doi.org/10.1088/0004-637X/793/2/132)
- Stone, J. M., Gardiner, T. A., Teuben, P., Hawley, J. F., & Simon, J. B. 2008, *ApJS*, 178, 137, doi: [10.1086/588755](https://doi.org/10.1086/588755)
- Valdivia, V., Hennebelle, P., Gérin, M., & Lesaffre, P. 2016, *A&A*, 587, A76, doi: [10.1051/0004-6361/201527325](https://doi.org/10.1051/0004-6361/201527325)
- Vázquez-Semadeni, E., Banerjee, R., Gómez, G. C., et al. 2011, *MNRAS*, 414, 2511, doi: [10.1111/j.1365-2966.2011.18569.x](https://doi.org/10.1111/j.1365-2966.2011.18569.x)
- Wolfire, M. G., Hollenbach, D., & McKee, C. F. 2010, *ApJ*, 716, 1191, doi: [10.1088/0004-637X/716/2/1191](https://doi.org/10.1088/0004-637X/716/2/1191)